The influence of freestream turbulence on the development of a wind turbine wake

Stefano Gambuzza† and Bharathram Ganapathisubramani

Aerodynamics and Flight Mechanics Research Group, University of Southampton, Southampton SO17 1BJ, United Kingdom

(Received xx; revised xx; accepted xx)

The wake of an isolated model-scale wind turbine is analysed in a set of inflow conditions having freestream turbulence intensity between 3 % and 12 %, and integral timescales in the range of 0.1 to 10 times the convective timescale based on the turbine diameter. It is observed that the wake generated by the turbine evolves more rapidly, with the onset of the wake evolution being closer to the turbine, for high turbulence intensity and low integral timescale flows, in accordance with literature, while flows at higher integral timescales result in a slow wake evolution, akin to that generated by low-turbulence inflow conditions despite the highly-turbulent ambient condition. The delayed onset of the wake evolution is connected to the stability of the shear layer enveloping the near wake, which is favoured for low-turbulence or high-integral timescale flows, and to the stability of the helical vortex set surrounding the wake, as this favours interaction events and prevents momentum exchange at the wake boundary which hinder wake evolution. The rate at which the velocity in the wake recovers to undisturbed conditions is instead analytically shown to be a function of the Reynolds shear stress at the wake centreline, an observation that is confirmed by measurements. The rate of production of Reynolds shear stress in the wake is then connected to the power harvested by the turbine to explain the differences between flows at equivalent turbulence intensity and different integral timescales. The wake recovery rate, and by extension the behaviour of the turbine wake in high-integral timescale flows, is seen to be a linear function of the freestream turbulence intensity for flows with Kolmogorov-like turbulence spectrum, in accordance with literature. This relation is seen not to hold for flows with different freestream turbulence spectral distribution; however, this trend is recovered if the contributions of low frequency velocity components to the turbulence intensity are ignored or filtered out from the computation.

Key words:

1. Introduction

Wind turbines are machines that present a number of peculiar characteristics regarding their operation: firstly, these are situated in the lowermost portion of the atmospheric boundary

† Email address for correspondence: s.gambuzza@soton.ac.uk

layer, and thus harvest power from turbulent, sheared inflows. Moreover, to accommodate for the rising market demand in renewable energy, these are often grouped in wind farms that house a large number of these machines in a finite area: as a result, all turbines that are not situated in the first row of the wind farm experience, as incoming flow, a combination of the wakes of upstream machines and turbulent freestream entrained from the atmospheric boundary layer surrounding the farm. In particular, the presence of upstream machines limits the power that a wind turbine in the back rows of a farm can harvest, as it will harvest energy from a lower-momentum inflow (Frandsen and Barthelmie 2002; Barthelmie and Jensen 2010). For this reason, a good knowledge of the wake generated by a wind turbine in a complex, turbulent inflow is paramount to the prolonged development and deployment of wind energy around the world.

As mentioned, the environment in which wind turbines operate is turbulent and sheared: this is often parameterised with the freestream turbulence intensity, defined as

$$I_\infty = \frac{\sqrt{\overline{u'^2}}}{U_\infty}, \tag{1.1}$$

where U_∞ is the bulk freestream speed, and $\sqrt{\overline{u'^2}}$ is the standard deviation of the velocity time-history. Elliott and Cadogan (1990) report data showing that turbines in an on-shore environment are subject to $I_\infty < 15\,\%$ for 95 % of their operating life. Similarly, Wagner et al. (2011) and Peña et al. (2016) report that turbines at the Høvsøre on-shore testing site experience values of I_∞ between 2 % and 14 %, with a strong dependency on the wind direction: less turbulent inflows are observed for winds arising from the ocean. Turbulence intensity for offshore sites is usually lower, with values of I_∞ comprised between 6 % and 8 % (Barthelmie et al. 2005; Türk and Emeis 2010).

Wakes of wind turbines are complex in nature, being characterised by the superposition of a large number of events: in the simplest of descriptions, the time-averaged wake of a wind turbine is, sufficiently far from the turbine rotor, characterised by a self-similar velocity deficit profile having a Gaussian distribution in the stream-normal directions (Medici and Alfredsson 2006); this is in line with the wakes generated by other axisymmetric bluff bodies such as spheres (Uberoi and Freymuth 1970) or porous plates (Rind and Castro 2012a; Aubrun et al. 2019; Vinnes et al. 2022). Closer to the turbine, the actual shape of the velocity profile is dominated by the distribution of pressure around the turbine blades: although sometimes the velocity deficit distribution is constant along a radial direction (Medici and Alfredsson 2006; Mycek et al. 2014; Lignarolo et al. 2015), this need not necessarily be, especially for turbines that are not operating at on-design conditions (Vermeer et al. 2003; Carbajo Fuertes et al. 2018; Foti et al. 2018; Dasari et al. 2019). The transition from these arbitrary profiles to the self-similar Gaussian ones is understood to be a function of the freestream turbulence intensity (Medici and Alfredsson 2006; Ishihara and Qian 2018). This region of lower velocity is separated from the surrounding freestream by an annular shear layer which is dominated by the presence of a helical vortex structure (Lissaman 1979; Crespo and Hernández 1996; Troldborg et al. 2010; De Cillis et al. 2020): this is analogous to the classical horseshoe vortex characteristic of finite wings generating lift, and it takes a helical structure due to the rotation of the blades as freestream convects these vortices downstream. The stability of this structure has been connected to the onset of wake evolution (Lignarolo et al. 2014, 2015), where a strong shear layer enveloping the wake inhibits it; moreover, the stability (or lack thereof) is also seen to drive a low-frequency motion of the wake in the stream-normal directions, named wake meandering (Medici and Alfredsson 2006; Heisel et al. 2018; De Cillis et al. 2020), with this motion being favoured by unstable shear layers. In general, an increase in the freestream turbulence intensity is seen to hasten the transition

to a self-similar velocity profile (Medici and Alfredsson 2006) and a smaller velocity deficit at a given distance from the turbine (Bastankhah and Porté-Agel 2014; Christiansen and Hasager 2005; Chamorro et al. 2012); this is seen from the point of view of a wind farm operator as a larger distance necessary between turbines in an offshore environment, as the lower freestream turbulence intensity of those sites does not favour wake recovery as much as in on-shore sites (Christiansen and Hasager 2005). The stability of the shear layer is also seen to be related to the freestream turbulence intensity, shown by Sørensen et al. (2015) as a relationship between the breakdown of the helical vortex structure and I_∞.

Often, the wake generated by the turbine is divided in a near and a far wake region, with the former being characterised by the presence of the helical vortex structure and a non-self-similar velocity profile, while the latter shows opposite characteristics. The division of the wake in a near and far field is commonplace for wakes generated by all bluff bodies, and goes back to the first works by Castro (1971) and Pope and Whitelaw (1976). Attempts to define the location of the boundary between the near and the far wake have been, in recent times, published by a number of authors: for instance, Sørensen et al. (2015) defines the boundary as the point of inflection of the turbulent kinetic energy content of some selected POD modes in the turbine wake. De Cillis et al. (2020) instead defines the boundary to be the location for which the time-averaged turbulent kinetic energy in the wake falls below a given threshold. Wu and Porté-Agel (2012) uses instead the change in sign in the turbulent kinetic energy advection term. Authors such as Howard et al. (2015) and Kang et al. (2014) instead connect the onset of wake meandering to the transition from near to far wake: Kang et al. (2014) show, from LES around a turbine, that the root-vortex set undergoes instability, starting meandering in the near wake; as this motion reaches the annular shear layer around the turbine, it favours its breakdown and the full transition to a far-wake, which is confirmed by the experiments of Howard et al. (2015). Similar results are shown by Foti et al. (2018). Neunaber et al. (2020) instead proposes a more complex definition of the turbine wake, which places two intermediate regions, named transition and decay regions, between the near- and far-wake; according to the authors, the near-wake is characterised by the presence of homogeneous and isotropic turbulence at its centre, unlike the other regions where the nacelle influence is still observed on the turbulence statistics. In all cases, transition to the far-wake is hastened by a more turbulent freestream. It can be understood that, given the differences between these methods, the location of the transition each model gives is different from that of any other model. This is to be expected as near- and far-wake are terms that describe the absence or presence of a large set of events, which need not appear or disappear simultaneously; as such, the distinction between near and far wake ad the estimation of this transition can only be qualitative.

It can be understood that not all these phenomena in the wake are of interest to a wind turbine operator: for this reason, engineering applications usually treat the wake statistically in a simplified form, often ignoring some of the aspects here described. Analytical wake models are engineering tools often used to predict the wake generated by wind turbines; these often relate the flow velocity in the turbine wake to some global parameters, simple to measure or estimate. The model that has seen the most widespread use in literature in the last years is the Gaussian wake model (Bastankhah and Porté-Agel 2014): according to this, one has that the velocity deficit in the turbine wake is given by

$$\frac{\Delta U}{U_\infty} = \frac{U_\infty - U}{U_\infty} = \left(1 - \sqrt{1 - \frac{C_T}{8(\sigma_w/D)^2}}\right) \exp\left(-\frac{1}{2(\sigma_w/D)^2}\left(\frac{r}{D}\right)^2\right), \tag{1.2}$$

$$\frac{\sigma_w}{D} = \epsilon + k^* \frac{x}{D}, \tag{1.3}$$

where U_∞ is the freestream speed, U is the velocity in the wake function of the streamwise distance from the turbine x and the radial distance away from the turbine axis r, D is the turbine radius, C_T is the thrust coefficient, ϵ is a known function of C_T and k^* is a parameter related to the spatial growth of the wake. The effect of turbulence, which has been seen to be for other bluff-bodies that of hastening the wake development and shortening the wake, is often represented as a change in the wake recovery rate k^*. Niayifar and Porté-Agel (2016) report an elaboration of LES data of the wake generated by a commercial turbine, showing a linear relationship between the freestream turbulence intensity and the wake recovery rate, for a constant value of C_T; this is also observed by Carbajo Fuertes et al. (2018) with field data on the wake of a turbine acquired with LiDAR. For the similar Jensen wake model (Jensen 1983), Peña et al. (2016) show that the wake recovery rate is a linear function of the freestream turbulence intensity if one assumes an inflow that is modelled with Monin-Obukhov similarity theory (Monin and Obukhov 1954). However, some works in recent literature have outlined how the predictions of wake models can be better tuned by introducing one additional parameter: for instance, Neunaber et al. (2022) shows that the accuracy of the predictions of commonly-used wake models can be improved by introducing a virtual origin in their equations. This practice, commonplace when treating wakes of bluff bodies, is seldom carried out in wind engineering. In this work, the authors measure the wakes of two model-scale wind turbines, subject to either a laminar inflow or to the wake of an upstream machine. Their data shows that the addition of a virtual origin in analytical wake models can improve the quality of the predictions for the wake of downstream machines, hinting to the conclusion that a virtual origin might include information on the inflow conditions. However, data included in their paper only consists of the wakes generated under either a laminar inflow or the wake of another turbine: given the large range of turbulent flows that turbines experience, it is important to observe whether a virtual origin can improve on the predictions of analytical wake models for an arbitrary inflow condition, and what its physical meaning is. While a large body of literature has been dedicated to understanding the effects of freestream turbulence intensity on the wake and on analytical prediction, little has been done to characterise the wake developed by a turbine in the presence of flows with different spectral content of turbulence. It is well established that the distribution of inflow turbulence affects the near-wake and the power a wind turbine generates (Sheinman and Rosen 1992; Tobin et al. 2015; Chamorro et al. 2015; Deskos et al. 2020; Li et al. 2020; Gambuzza and Ganapathisubramani 2021) and the drag generated by turbine simulators (Blackmore et al. 2014), with turbines being more apt at converting velocity fluctuations into power if those are present as lower-frequency contributions. Most works in literature therefore highlight how a wind turbine acts as a low-pass filter when converting inflow into mechanical power. It can thus be assumed that the wake generated by a turbine in flows with different representations in the frequency domain are characterised by different scales, and indeed some works report different spectral composition between the freestream and the wake generated by the turbines (Tobin and Chamorro 2019; Heisel et al. 2018). In addition, Chatterjee and Peet (2018, 2021) show that, from LES of an infinite wind farm, the mechanism of mean kinetic energy entrainment from the freestream to the wake is favoured in the presence of very-large-scale structures, with sizes of approximately 10 times the turbine diameter. Their work shows that the presence of a turbine effectively remodulates the spectral content of the wake, favouring large-scale motions in the wake. Whether this leads to different mechanisms of wake development is an assumption that has seldom been tested in literature for an isolated turbine, and indeed engineering models do assume no effect of the turbulence spectrum on the wake evolution, with parameters such as k^* being only function of I_∞. For this reason, this paper aims to investigate the relationship between the changing inflow conditions that a turbine is subject to and the mechanisms that regulate and dominate the development of

this wake. We follow on our previous work in (Gambuzza and Ganapathisubramani 2021) and carry out an experimental study to characterise the wake of a model-scale turbine under different inflow turbulence conditions.

This paper is structured as follows: section 2 will briefly present the experimental methodology used to collect the data here presented, along with its shortcomings. Section 3 will present the results obtained: this chapter is further divided in three subsections, which will relate more in detail to the predictions of engineering models (section 3.1) and to the physics behind the trends observed (section 3.2 and section 3.3). Section 4 will summarise these findings concisely.

2. Experimental method

This paper reports the measurements of velocity in the wake of a model-scale wind turbine, measured via planar PIV in a wind tunnel equipped with an active turbulence generating grid. This section will expand on the experimental methodology that has been employed to obtain the results reported in the remainder of the paper, outlining the main characteristics and the limitations of the techniques employed. Some of the techniques utilised in this study are described in more detail in the previous study published in Gambuzza and Ganapathisubramani (2021).

2.1. *Facility*

The experiments have been carried out in the 3×2 boundary layer wind tunnel at the University of Southampton. This is a suction wind tunnel having a rectangular cross-section of size $0.9 \times 0.6\ \mathrm{m}^2$, and a total usable length of constant cross-section of 4.5 m. Flow is driven by a fan placed downstream of the test section, and flow conditioning is carried out by a set of honeycomb meshes upstream of a contraction that leads to the test section. During the tests here described, the wind tunnel has been equipped with a turbulence-generating active grid, designed to the specifications of Makita (1991), which is able to generate turbulent flows with different level of shear and freestream turbulence intensities up to 16 % (Hearst and Ganapathisubramani 2017; Li et al. 2020); no shear has been generated for the measurements presented in this study. This grid is composed of 18 stepper motors that independently drive 11 vertical rods and 7 horizontal rods, each moving a set of agitator wings. The mesh spacing between rods M is 81 mm. The grid is operated by changing the angular velocity of each rod to a random value in a predetermined interval, with rods allowed to cruise to speed for a limited time before changing direction and speed: this actuation procedure is in detail described by Poorte and Biesheuvel (2002) as double-random mode. The active grid is situated at the inlet of the wind tunnel test section, with the rods covering the whole of the wind tunnel cross-section.

During the tests, the wind tunnel fan has been operated to generate a mean freestream speed U_∞ equal to 8 m/s. This has been measured by means of a Pitot probe placed $2.5M$ upstream of the active grid. To account for the change in U_∞ along the test section, this has been calibrated to a Pitot placed at the same location as the turbine in an otherwise empty test section.

2.2. *Model-scale turbine*

The turbine used during these tests is a speed controlled, fixed pitch model-scale wind turbine, having a rotor of diameter D equal to 0.18 m. For this value of D and the aforementioned constant value of U_∞, the diameter-based Reynolds number of these tests is $Re = 9.6 \times 10^4$. Data reported by Chamorro et al. (2012) show that this is sufficiently high to attain Reynolds-independent results both in the mean and the second moment of the wake velocity signals.

r/r_{tip}	c/r_{tip}	β [deg]	Aerofoil
0.13	0.13	58.20	NACA 63-418
0.20	0.27	35.58	NACA 63-418
0.30	0.26	24.13	NACA 63-418
0.40	0.24	16.76	NACA 63-418
0.50	0.22	11.77	NACA 63-418
0.60	0.21	8.22	NACA 63-418
0.70	0.19	5.58	NACA 63-418
0.80	0.17	3.55	NACA 63-418
0.90	0.16	1.94	NACA 63-418
1.00	0.14	0.64	NACA 63-418

Table 1: Turbine geometry, defined as the distribution of chord c, twist β and aerofoil shape along the blade span coordinate r.

The turbine rotor has been directly connected to a brushed permanent magnet DC machine that has been used as a generator to brake the rotor while operating. This has not been connected to other sources of mechanical or electrical power, with the only torque acting on the turbine shaft being the one generated by the freestream on the turbine blades, and the power generated being transformed into heat dissipated by the motor. The turbine nacelle has been supported by an aluminium mast of diameter 15.75 mm, which has placed the centre of the rotor at the centre of the test section. The turbine has then been located at a streamwise distance of $36M = 16D$ downstream of the active grid. The geometry of the blade, defined as the distribution of chord and twist along the blade span, is reported in table 1, where $r_{\text{tip}} = D/2$ is the spanwise location of the last section of the blade. The turbine blade is designed to harvest maximum power from the incoming flow at a tip-speed ratio λ of 4; this parameter is defined as

$$\lambda = \frac{\omega\, r_{\text{tip}}}{U_\infty}, \tag{2.1}$$

where ω is the turbine rotor angular velocity.

2.3. *Planar particle image velocimetry*

In this study, planar PIV has been employed to measure the velocity in the turbine wake on a stream-parallel vertical plane; the out-of-plane velocity component is not measured by this technique. The nomenclature that is used in the remainder of the paper defines x to be the streamwise coordinate, positive in the direction of the flow, and y to be the stream-normal, vertical coordinate, positive upwards; both are dimensional and are adimensionalised by the turbine diameter D. The origin of this reference frame is placed at the centre of the turbine rotor, so that x defines the streamwise distance from the rotor-swept plane, and y measures the distance from the turbine axis of rotation. The convention used here employs the label u for the streamwise component and v for the vertical component of velocity; both are made adimensional by the freestream speed U_∞. Moreover, Reynolds decomposition is used to separate the velocity into a time-averaged and a fluctuating, zero-mean component:

$$u(t) = \overline{u(t)} + u'(t) = U + u'(t), \tag{2.2}$$

where the overline denotes time-averaging, a capital letter represents a quantity constant in time and the prime symbol denotes a signal having zero time-mean.

Figure 1 reports a schematic representation of the planar PIV setup used during this study.

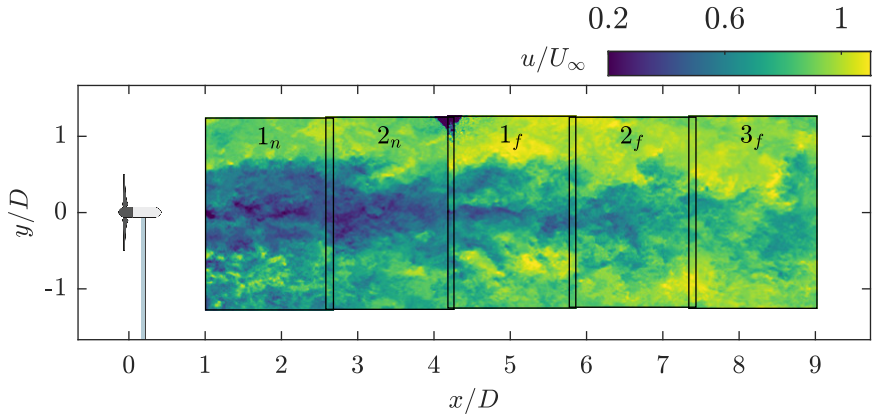

Figure 1: Planar PIV setup with the cameras fields of view in the near wake (1_n and 2_n) and in the far wake (1_f, 2_f, and 3_f), including an instantaneous estimate of the streamwise velocity in the turbine wake. All dimensions to scale.

Three Imager Pro LX cameras have been used to obtain the five fields of view reported in figure 1, which have been illuminated by a Litron Bernoulli PIV laser: initially, two cameras have simultaneously acquired the velocity field for streamwise distances of 1 to 4.2 rotor diameters downstream of the turbine; these are indicated as positions 1_n and 2_n in the figure. Subsequently, these cameras have been moved, and a third camera has been added to acquire between 4.1 and 9 diameters of downstream distance; these are locations 1_f to 3_f. All cameras fields of view have dimensions of 300 mm in the x-direction and 450 mm in the y-direction in object-plane units, or 1.67×2.5 rotor diameters; all fields of view overlap the previous and next by a strip 15 mm wide and 450 mm tall, which allows for the statistics fields to be stitched together along the whole span of the measurement domain. Moreover, instantaneous velocity fields are stitched between cameras 1_n and 2_n, as these have acquired simultaneously, and between cameras 1_f to 3_f for the same reason. Processing of the PIV particle displacement snapshots is carried out with LaVision DaVis, specifying an initial window size of 96×96 px and a final window size of 48×48 px with a 75 % overlap between adjacent windows: this results in an overall vector spacing of 1 velocity vector per 1.1 mm in both the x- and y-directions, or 162 vectors in one rotor diameter. Due to the large magnification factor that had to be employed to image the fields of view, tracking particles had a size of approximately 1 px in image-plane units, which lead to the phenomenon of peak-locking as described by Christensen (2004). To alleviate the effect of this on the computed statistics, the histogram normalisation correction algorithm presented by Hearst and Ganapathisubramani (2015) has been applied to all correlation maps in image-plane units of displacement, prior to the application of a calibration to convert these into object-plane units of velocity. The velocity fields have been acquired at a frequency of 0.6 Hz: for a freestream speed of 8 m/s, this corresponds to a displacement in the free-stream of 74 diameters of the wind turbine, equal to the length of the wind tunnel test section; for this reason, the velocity realisations are assumed to be statistically independent. Velocity snapshots have been phase-locked to the instantaneous position of the turbine rotor, to ensure a uniform distribution of all phases in the computed statistics; this has been realised by timing the laser discharge to the index signal of a rotary encoder installed on the turbine shaft. A total of six phases have been recorded, at a distance of 0°, 20°, 40°, 60°, 80°, and 100° from the reference rotor position; as the turbine rotor has three blades, the resulting velocity field is understood to be periodic to a 120° rotation of the turbine rotor. A total of 300 instantaneous snapshots of velocity have

λ	C_T
1.9	0.52
3.8	0.76
4.7	0.80

Table 2: Turbine thrust coefficient C_T as a function of the tip-speed ratio λ for the operating conditions presented in this study.

been acquired for each phase: unless otherwise mentioned, statistics are computed on the full dataset consisting of 1800 snapshots per test case. Uncertainty in the instantaneous velocity measurements has been estimated by DaVis to be equal to 1.5 % of the measured values in the near wake fields of view and 1.0 % in the far wake fields, with these values being constant between test cases. This is estimated following the method presented in Wieneke (2015).

2.4. *Test cases*

The turbine wake has been generated under 18 different conditions: these are parameterised with the operating tip-speed ratio of the turbine and the freestream turbulence conditions that the turbine has been subject to. The turbine has been operated at three distinct values of tip-speed ratio λ: these are $\lambda = 1.9$, for which the turbine generates low power and thrust, and the flow around the blades is mostly stalled; $\lambda = 3.8$, for which the turbine generates the most power; and $\lambda = 4.7$ at which the thrust generated is at its maximum. Curves of power and thrust generated by the turbine have been previously reported by Gambuzza and Ganapathisubramani (2021) as adimensional power and thrust coefficients (respectively C_P and C_T): these are defined as

$$C_P = \frac{Q\,\omega}{\frac{1}{2}\rho U_\infty^3 \pi r_{\text{tip}}^2}, \tag{2.3}$$

$$C_T = \frac{T}{\frac{1}{2}\rho U_\infty^2 \pi r_{\text{tip}}^2}, \tag{2.4}$$

where Q is the torque generated by the rotor, ω is its angular velocity, and the product of these quantities is the mechanical power harvested by the turbine, T is the turbine thrust, and ρ is the air density. The values of C_T generated by the turbine for the different λ at which it has been operated are listed in table 2: as reported in Gambuzza and Ganapathisubramani (2021), little effect of the freestream turbulence characteristics is seen on these values.

The active grid has been used to generate six different freestream turbulence conditions: in this work, these are classified based on their turbulence intensity

$$I_\infty = \frac{\sqrt{\overline{u'^2}}}{U_\infty}, \tag{2.5}$$

and their integral timescale T_0, computed as

$$T_0 = \int_0^{\tau_0} \rho_{uu}(\tau)\, d\tau, \tag{2.6}$$

where $\rho_{uu}(\tau)$ is the autocorrelation coefficient of $u'(t)$ and τ_0 is the first value of τ for which $\rho_{uu}(\tau) = 0$. This last quantity is presented in the remainder of the paper as normalised by the convective timescale D/U_∞. To compute both I_∞ and T_0, hot-wire anemometry has

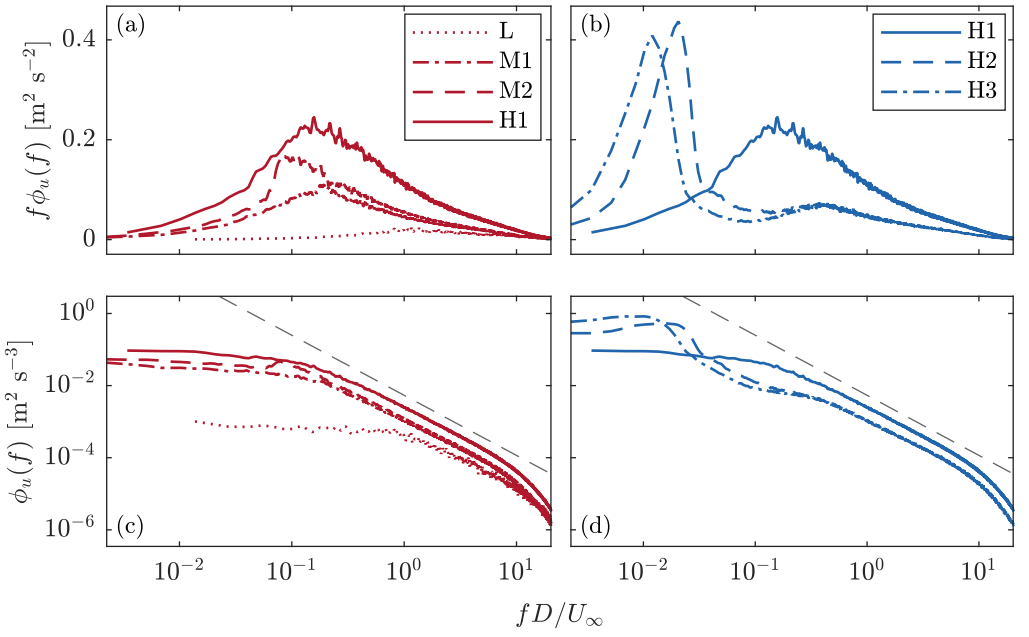

Figure 2: Top row: spectra of the streamwise component of freestream turbulence $\phi_u(f)$ premultiplied by the frequency axis *versus* adimensional frequency for flows at integral timescale $T_0 \leqslant 1$ (Kolmogorov-like flows, *a*) and flows at equivalent turbulence intensity I_∞ (non-Kolmogorov flows, *b*). Bottom row: same spectra plotted as non-premultiplied on canonical log-log axes along with -5/3 slope (*dashed grey*).

Name	L	M1	M2	H1	H2	H3
U_∞ [m/s]	8.0	8.0	8.0	8.0	8.0	8.0
I_∞ [%]	3.0	7.5	8.8	11.5	11.3	11.6
T_0	0.1	0.9	1.0	1.0	6.3	10.5
Ro	-	2	5	2	40	60
Wings	-	P	P	F	P	P

Table 3: Freestream turbulence characteristics of the generated inflow conditions, and active grid operating parameters (F: full wings; P: pierced wings).

been used to measure the freestream velocity in an otherwise empty test section, on a 5×2 grid at the centre of the test section spanning the rotor-swept area: more details on the hot-wire anemometry setup is included in Gambuzza and Ganapathisubramani (2021). The characteristics of the six flows generated are summarised in table 3: these are named L for the low-turbulence test case, M1 and M2 for the medium I_∞ and H1 to H3 for the high turbulence intensity test cases.

The freestream turbulence spectra are presented in figure 2: in this, the flows are divided in two families, one exhibiting the canonical distribution of energy in the spectrum of Kolmogorov (1941), which are reported in figure 2(a, c) and are characterised by $T_0 \leqslant 1$, and a second for which freestream turbulence intensity I_∞ is approximately constant, but the distribution of this does not follow that of the Kolmogorov spectrum, showing a marked spectral gap for adimensional frequencies around 1×10^{-1} and a narrowband contribution at

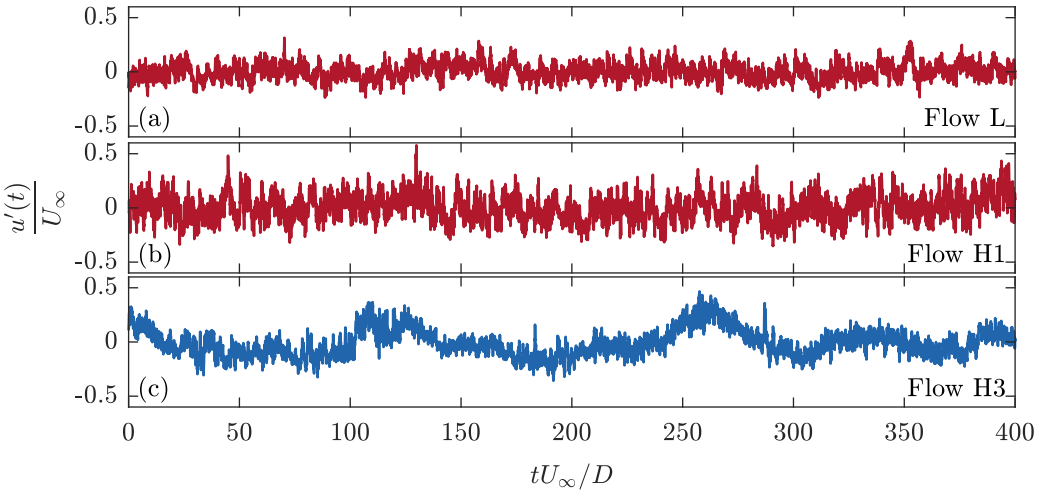

Figure 3: Time-series of freestream velocity $u(t)$ for three selected test cases, plotted *versus* time normalised by the convective timescale $\frac{D}{U_\infty}$.

low frequencies. This can be, for instance, thought to be analogous to the meso-scale peak observed in the spectrum of the atmospheric boundary layer (der Hoven 1957; Smedman-Högström and Högström 1975), although the ratio between the frequency of this peak and the start of the inertial subrange is approximately one order of magnitude, instead of the three-to-four orders seen in literature. Flows H2 and H3 are thus labelled non-Kolmogorov-like flows in the remainder of the text. This is a desired feature, as previous studies of wind turbine wakes in turbulence employ turbulence whose spectra is Kolmogorov-like (Chamorro and Porté-Agel 2009; Barlas et al. 2016; Deskos et al. 2020; Neunaber et al. 2021). As it was discussed in section 1, this is often an assumption that is not challenged in literature, namely that the distribution of power in the incoming turbulence spectrum does not affect the development of a wind turbine wake. Note that, while flows H2 and H3 exhibit a large value of T_0, it would be incorrect to assume those are the result of very-large-scale structures: assuming Taylor's hypothesis to hold true, an estimate for the large-eddy size can be given by

$$L_0 = T_0\, D, \tag{2.7}$$

which for flow H3 results in an approximate value of 1.8 m, or twice the test-section width and three times the test section height. It must therefore be accepted that, for flows H2 and H3 presented here, Taylor's hypothesis need not hold as the high integral timescale of these flows is instead representative of a low-frequency change in the bulk freestream velocity as seen by the turbine. In practical terms, these non-Kolmogorov-like flows are generating by actuating the motion of the active grid agitator wings at lower speeds than those used for Kolmogorov-like flows: this can be quantified introducing the grid Rossby number Ro, defined as

$$Ro = \frac{U_\infty}{\Omega M}, \tag{2.8}$$

where Ω is the mean angular velocity of the active grid rods. For the two non-Kolmogorov-like test cases, the slow rotation of the rods translates into a slow change of the blockage generated by the grid, which in turn induces slow changes in the bulk freestream speed. This can be easily appreciated from the time-series of velocity reported in figure 3.

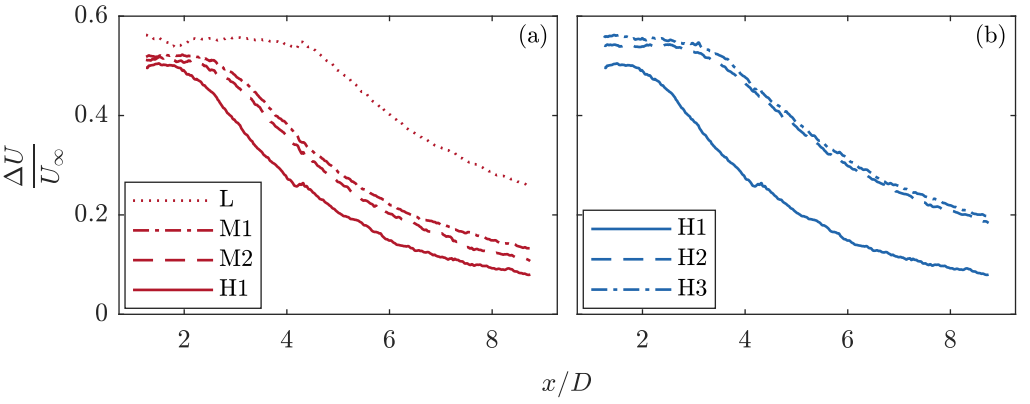

Figure 4: Maximum velocity deficit $\Delta U/U_\infty$ as a function of the streamwise distance from the turbine x/D for the Kolmogorov-like flows at $T_0 \leqslant 1$ (*a*) and for the equivalent I_∞ flows (*b*). Turbine operating at peak power-generating $\lambda = 3.8$.

3. Results and discussion

As briefly introduced in section 1, one of the most important parameters of the turbine wake is the velocity deficit ΔU. This is defined as a function of the streamwise distance from the turbine as

$$\frac{\Delta U}{U_\infty} = \frac{U_\infty - \min_y(U(x,y))}{U_\infty}, \tag{3.1}$$

where the dependency of U on y is removed by taking the minimum in that direction. This parameter is of interest to a wind farm designer as this sets the streamwise distance between rows of turbines in a wind farm.

Figure 4 reports the trends of the velocity deficit ΔU for all inflow conditions analysed in this study. In particular, figure 4(a) isolates the trends for the Kolmogorov-like flows: it can clearly be seen that an increase in the freestream turbulence intensity generates a monotonic decrease of the velocity deficit, and therefore a faster wake recovery and a shorter overall wake length. This is often connected to an increase in the turbulent mixing, favouring the homogenisation of velocity between the low-speed wake and the higher-momentum freestream surrounding it (Medici and Alfredsson 2006; Chamorro and Porté-Agel 2009), a behaviour that is also seen for other bluff-bodies in turbulence (Hearst et al. 2016). On the other hand, figure 4(b) instead collects the family of flows at equivalent I_∞, and even in this case important differences between the wake velocity profiles are seen. In particular, the wakes generated for the non-Kolmogorov-like flows H2 and H3 are seen to be only slightly different, and these appear to evolve more slowly both with respect to the equivalent-I_∞ flow H1, and more surprisingly to flow M1, which has a much smaller value of freestream turbulence intensity. In fact, only the wake generated under flow L, which here has been taken as reference for a low-turbulence flow, evolves more slowly.

Data reported in the previous figure 4 has been obtained by fixing the turbine tip-speed ratio and, ultimately, its thrust. However, figure 5 reports the value of $\Delta U/U_\infty$ for all flows the turbine has been subjected to and for all three values of C_T here studied; freestream turbulence intensity is reported on the horizontal axis and freestream integral timescale is reported as colour of the markers. It can clearly be seen that the results of figure 4 can be generalised to all values of C_T here studied, and thus these are representative of a peculiar behaviour of the wind turbine. The trend of velocity deficit with turbulence intensity, limiting the analysis to the Kolmogorov-like flows of $T_0 \leqslant 1$, is clearly decreasing; as no data has

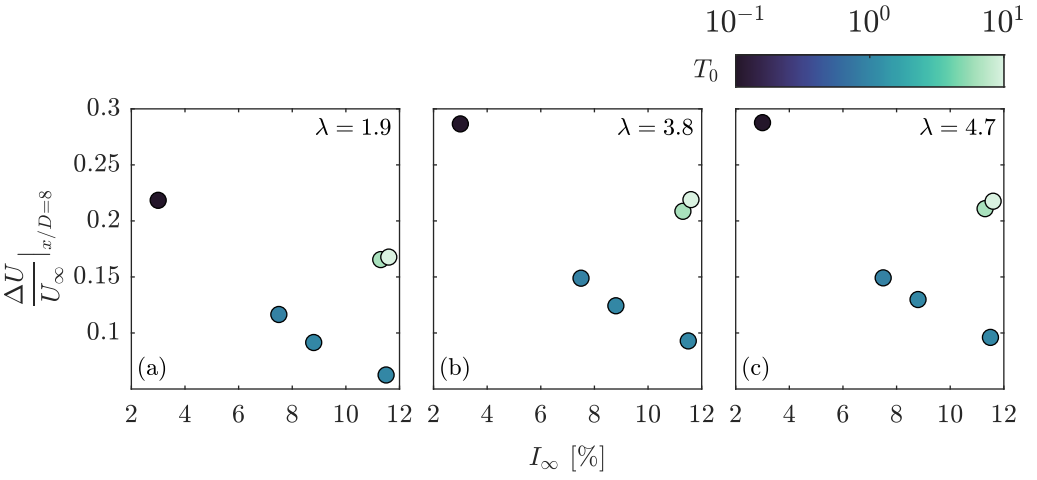

Figure 5: Velocity deficit $\Delta U/U_\infty$ at $x/D = 8$ for all operating conditions, as a function of the freestream turbulence intensity I_∞ (horizontal axis) and integral timescale T_0 (colour, note the logarithmic axis), for the turbine operating at $\lambda = 1.9$ (*a*), $\lambda = 3.8$ (*b*) and $\lambda = 4.7$ (*c*).

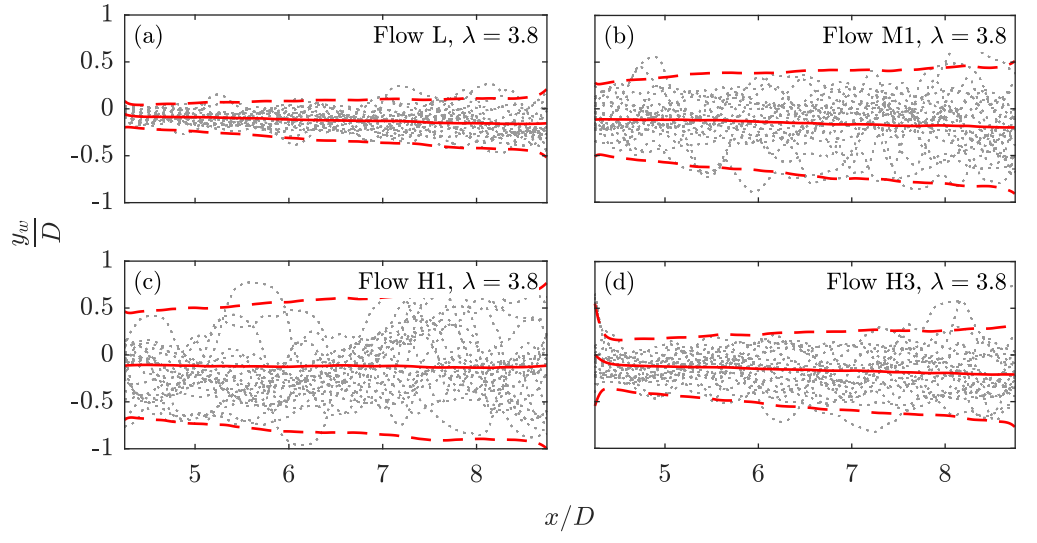

Figure 6: Instantaneous trajectory of the wake $y_w(x)$ (dotted grey lines, 20 random trajectories shown per test case), alongside mean wake trajectory (solid red line) and boundaries of the wake meandering region (dashed red lines). Data shown for inflow L (*a*), M1 (*b*), H1 (*c*) and H3 (*d*); turbine operating at $\lambda = 3.8$ for all four subfigures.

been acquired for values of $I_\infty > 12\,\%$, it cannot be said whether this tends asymptotically to zero or not. This is an important distinction: an asymptotic trend to zero would suggest that the turbine wake can be arbitrarily shortened by a large enough value of freestream turbulence. On the other hand, a trend to a small but finite value would instead hint to a behaviour for which the mean flow in the wake is unaffected by an increase of I_∞ after a certain threshold, a behaviour that is similar to what observed for boundary layers generated in freestream turbulence (Sharp et al. 2009; Dogan et al. 2016).

Wakes of turbines are also seen to meander, that is, change their instantaneous trajectory.

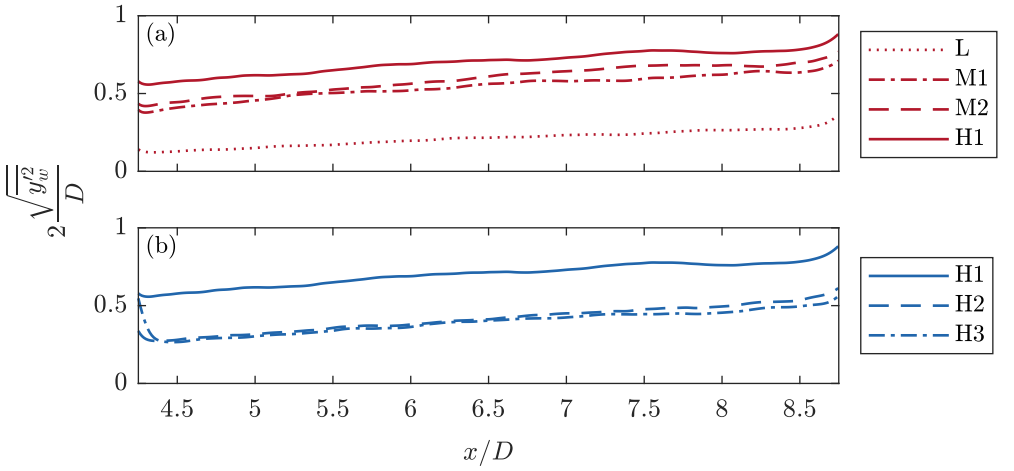

Figure 7: Extent of the meandering region estimated as twice the standard deviation of the instantaneous wake trajectories for the Kolmogorov-like flows at $T_0 \leqslant 1$ (*a*) and the flows at equivalent I_∞ (*b*). Turbine operating at $\lambda = 3.8$.

This is a phenomenon that is understood to be driven primarily by instabilities in the shear layer (Heisel et al. 2018); in the field, instantaneous changes in wind direction also contribute to this motion, a behaviour that is not simulated here. To identify the instantaneous trajectories of the wake from the individual velocity snapshots, the method from Howard et al. (2015) is used: in this, the instantaneous wake trajectory is determined for each x as

$$y_w(x,t) = \underset{y}{\operatorname{argmin}}(u(x,y,t)), \tag{3.2}$$

which is then low-pass filtered to remove all contributions having a wavelength smaller than $D/2$. Figure 6 reports, for each of the edge cases at $\lambda = 3.8, 20$ randomly chosen instantaneous trajectories in dotted grey. Alongside these, the mean wake trajectory is found by averaging the instantaneous y_w in time, and the extent of the meandering region is reported as twice the standard deviation of the instantaneous wake trajectories. Figure 7 reports instead the standard deviation of y_w in time for any given value of x/D. Assuming that the distribution of y_w for a given x/D is Gaussian, the point of minimum velocity in the wake is within the bounds

$$\left[\frac{\overline{y_w}}{D} - 2\frac{\sqrt{\overline{y_w'^2}}}{D}; \frac{\overline{y_w}}{D} + 2\frac{\sqrt{\overline{y_w'^2}}}{D}\right] \tag{3.3}$$

in 95 % of all observations, and therefore this value is representative of the extent of the wake meandering motion in space. It can be appreciated that the width of this region increases both with distance from the turbine, a phenomenon observed for the wakes of solid and porous disks by España et al. (2011) and in LES of wind farms by Foti et al. (2019), and with the freestream turbulence intensity content I_∞. Once again, by limiting the analysis to the Kolmogorov-like flows and the extent of the wake meandering region (see data reported in figure 7(a)), it is easy to appreciate that the extent of the wake meandering increases with the freestream turbulence content; that is, the wake meandering amplitude increases with increasing I_∞. However, the largest increase happens between flows L and M1, in conjunction with the increase in integral timescale of the flow T_0, suggesting that this is mostly due to the size of the eddies introduced in the freestream; adding more turbulence without affecting its

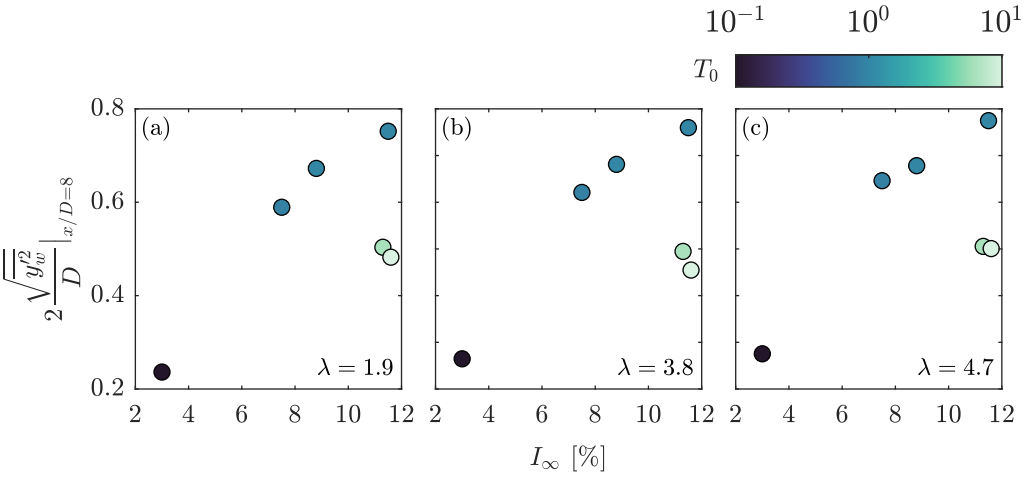

Figure 8: Extent of the meandering region at $x/D = 8$ as a function of the inflow conditions, for $\lambda = 1.9$ (*a*), $\lambda = 3.8$ (*b*), and $\lambda = 4.7$ (*c*).

scales increases the extent of meandering by inducing shear layer instabilities (Medici and Alfredsson 2006), although its effects are of smaller intensity when compared to those of mean-flow convection. On the other hand, the non-Kolmogorov flows H2 and H3 are seen to result in little wake meandering whose extent is, like for the velocity deficit, lower than that generated by flow M1 but higher than that of the low-turbulence flow L. This is despite a large value of T_0 that should suggest eddies 5 to 10 times larger between these flows and the equivalent-I_∞ flow H1; however, one must remember the remark given in section 2.4, for which Taylor's frozen hypothesis need not hold for the high-T_0 flows and the large value of T_0 is not necessarily representative of the large scale structure size. This can readily be seen by extracting the value of the wake meandering amplitude at $x/D = 8$, which is shown in figure 8: the largest increase in the wake meandering amplitude is observed going from $I_\infty = 3\,\%$ to $I_\infty = 7.5\,\%$. While the wakes generated by the two non-Kolmogorov flows are characterised by meandering, their amplitude is only intermediate between those of flow L ($I_\infty = 3\,\%$) and flow H1 ($I_\infty = 11.5\,\%$), and lower than those of flows at intermediate I_∞, a finding that holds true at all values of tip-speed ratio here investigated.

In addition to the velocity deficit, the wake diameter is an important parameter as this sets the lateral spacing between turbines in a farm; its growth in the streamwise direction is often taken as representative of the wake recovery rate and thus of the extent of the wake in the streamwise direction (Jensen 1983; Frandsen et al. 2006). Figure 9 reports the wake diameter D_w measured for all investigated inflows with the turbine operating at $\lambda = 3.8$; as the presence of the mast affects the flow for $y/D < 0$, this is computed as twice the distance between the iso-line of $U = U_\infty$ and the mean wake trajectory $\overline{y_w}$, which itself is obtained by averaging the instantaneous wake trajectories shown in the previous figure 6. To highlight the large-scale trends, the trends of D_w are also low-pass filtered to remove contributions with wavelengths below $D/2$. The most immediate result that can be observed is that, for the investigated cases at $\lambda = 3.8$, little effect of the inflow is seen on the initial evolution of the wake and in particular of its slope: all flows except flow L result in wakes with similar diameters for $x/D < 4$. This is an important observation, as this means that inferring the wake recovery rate k from the wake diameter trend might lead to inaccurate estimations in the field. For the high-turbulence flow H1, one can even observe that the trend of D_w is not linear for all values of x/D, and instead plateaus after $x/D = 7$; while it could be argued

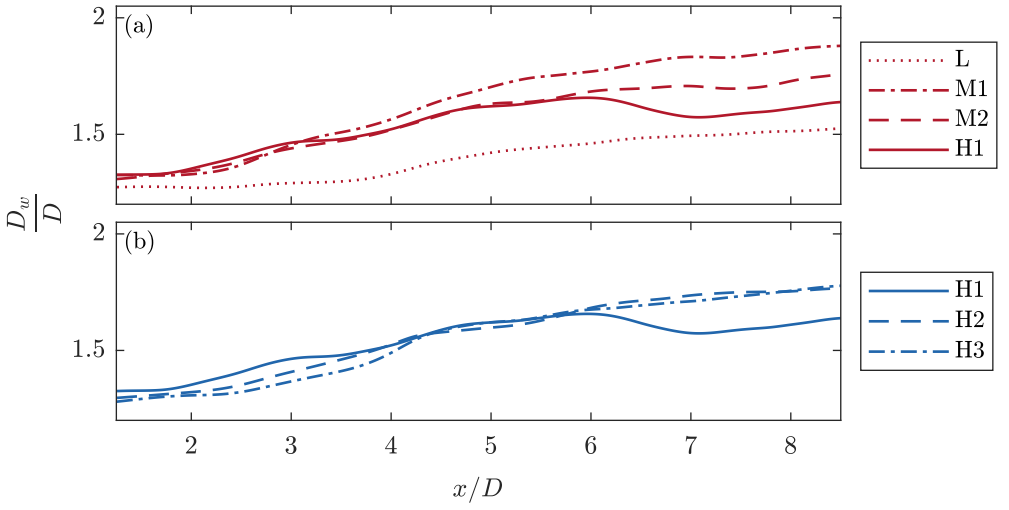

Figure 9: Adimensional wake diameter D_w/D measured at $\lambda = 3.8$, for inflows with $T_0 \leqslant 1$ (*a*) and flows at equivalent I_∞ (*b*).

that this is due to the presence of the wind tunnel walls, this does not seem to affect the evolution of all other wakes developed under different inflows, meaning the reason for this constant wake diameter might be found in the turbulence enveloping the wake. Following the approach of Pope (2000), one can observe that the momentum deficit flows is an invariant of the wake equal to the turbine thrust. The streamwise momentum equation can be written as

$$T = \rho \left(\int_{A_i} U_\infty^2 \, dA - \int_{A_w} U^2 \, dA \right), \tag{3.4}$$

where T is the turbine thrust, ρ is the fluid density, and A_i and A_w are two sections of a stream tube containing the wind turbine far upstream and downstream of the turbine respectively. As T is constant, so must be the product $U^2 \, dA$ on A_w; however, it can be seen from the data presented in figure 4(a) and figure 9(a) that for $x/D > 7$, D_w and therefore A_w is constant while U changes. It is at this point important to note that equation (3.4) only holds for A_w sufficiently downstream of the turbine, so that the mean momentum convection $U\frac{\partial U}{\partial x}$ dominates over the turbulent transport in both the streamwise and stream-normal directions $\frac{\partial \overline{u'^2}}{\partial x}$ and $\frac{\partial \overline{u'v'}}{\partial y}$ respectively. Data reported in section 3.3 will show that the case of flow H1 and $\lambda = 3.8$ is also the test case for which the terms of the Reynolds stress tensor are the largest; this, coupled with the fact that at $x/D \geqslant 7$, $U \simeq U_\infty$, drives $U\frac{\partial U}{\partial x}$ to low values, makes the assumptions under which equation (3.4) not necessarily hold.

The value of k can be obtained, as a function of the freestream turbulence characteristics, as the slope of the linear regression of D_w/D; to account for the plateau in D_w for the test case of flow H1 and $\lambda = 3.8$, the linear regression is performed for $x/D < 5$ for all test cases except for flow L. In the case of this flow, the regression is instead performed for $4 < x/D < 6$ to account for the initial plateau in D_w. Data reported in figure 10 shows that the trend of k is erratic with both turbulence intensity and integral timescale: for the low thrust case of $\lambda = 1.9$ (figure 10(a)) a somewhat linear trend of k with I_∞ is seen, with a small effect of T_0 on the wake expansion; this last observation is similarly seen for $\lambda = 3.8$, for which however the trend of k with I_∞ is not linear, and the wake that experiences the largest expansion is that developed under the moderate-turbulence of flow M1.

The data presented in this section therefore shows how the wake generated by the isolated

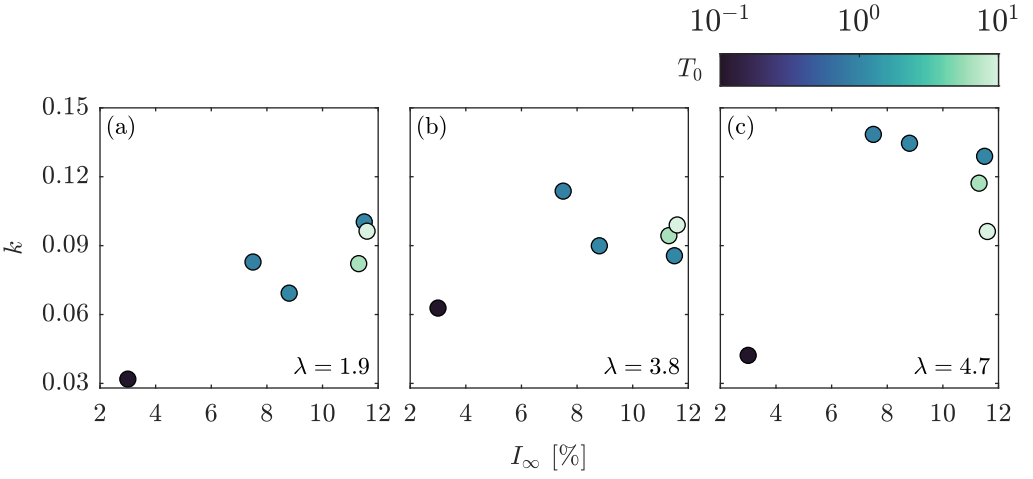

Figure 10: Wake growth rate k found as the slope of the linear regression of D_w/D; data for $\lambda = 1.9$ (*a*), $\lambda = 3.8$ (*b*) and $\lambda = 4.7$ (*c*). Data from subfigure (b) was already presented in figure 9.

turbine is affected by both the freestream turbulence intensity I_∞ and its frequency content, which in this study has been parameterised as its integral timescale T_0. However, the approach followed in this section has not attempted to quantify these effects, nor it has explained the physical phenomena that drive this evolution or these trends. The next section will therefore present a parameterisation of the wake generated by the wind turbine based on frequently used analytical wake models, which will then be leveraged in the next sections to quantify the effects of turbulence on the wake developed by the turbine.

3.1. *Quantifying the effects of turbulence*

As mentioned in section 1, analytical wake models are powerful tools that are often used both in literature and in the field to represent the complex turbine wake in a simplified fashion. These operate by assuming the existence of a relationship between the velocity in any point of the wake and a reduced set of parameters: for instance, the widespread Gaussian wake model, developed by Bastankhah and Porté-Agel (2014), assumes that the velocity in any point of the wake is described by the set of equations

$$\frac{\Delta U}{U_\infty} = \left(1 - \sqrt{1 - \frac{C_T}{8(\sigma_w/D)^2}}\right) \exp\left(-\frac{(r/D)^2}{2(\sigma_w/D)^2}\right), \tag{3.5}$$

$$\frac{\sigma_w}{D} = k^* \frac{x}{D} + \epsilon, \tag{3.6}$$

where r is the radial coordinate away from the turbine axis, k^* is a parameter that serves the role of the wake expansion rate k in the previous section. Regarding the definition of ϵ, the authors show that from considerations on the total mass flow deficit rate across the turbine disk one must have

$$\epsilon = 0.25\sqrt{\beta}, \tag{3.7}$$

where

$$\beta = \frac{1}{2}\frac{1 + \sqrt{1 - C_T}}{\sqrt{1 - C_T}}. \tag{3.8}$$

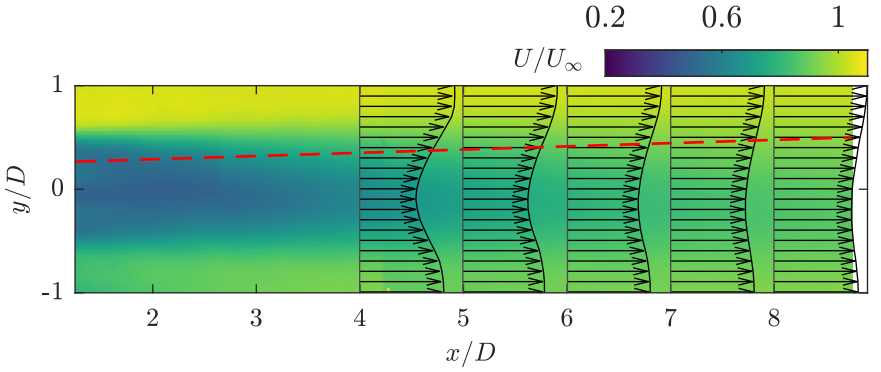

Figure 11: Determination of k^* from PIV measurements in the mean wake. In colour: mean streamwise velocity component; in black arrows: selected velocity profiles; in dashed red: linear regression of $\sigma_w(x)$. Data for flow M1, $\lambda = 3.8$.

However, the authors show that the Gaussian model provides estimates that better match LES data of turbines in the atmospheric boundary layer by assuming that $\epsilon = 0.2\sqrt{\beta}$. One must note that, as the authors explain, the difference between these formulations consists in the distance necessary for the wake to equalise its pressure with the surrounding free-stream: in particular, $\epsilon = 0.25\sqrt{\beta}$ assumes that this is verified on the turbine disc, while $\epsilon = 0.2\sqrt{\beta}$ assumes a non-zero distance necessary to attain this.

As full knowledge of the wake geometry is known from the PIV velocity fields, one can compute the value of k^* for each operating condition and inflow as outlined in figure 11: for every value of x/D, a velocity profile is obtained and fitted to a Gaussian profile, with the standard deviation of the fitted profile being an estimate of $\sigma_w(x)$. The value of k^* is then the slope of the linear regression of this last quantity. As for the previous data on the wake diameter D_w presented in figure 9, the fitting is limited to the range $0 < y/D < 1$ as the presence of the mast has impacted the symmetry of the wake; moreover, as the velocity profiles need not be Gaussian close to the turbine, especially at low values of I_∞ (Medici and Alfredsson 2006), σ_w is only computed for $x/D \geqslant 4$.

Figure 12(a) reports, for all wakes obtained at $\lambda = 3.8$ and thus constant $C_T = 0.76$, the trends of velocity deficit previously reported in figure 4 where the values on the horizontal axis are the distance from the turbine multiplied by the k^* attained in each specific operating condition: it can be appreciated that none of the curves collapse on the prediction that the Bastankhah and Porté-Agel (2014) offers. Figure 12(b) instead presents the velocity deficit trends where the distance from the turbine is normalised by k_0^*: this parameter is determined so that the velocity trends reported minimise, in a least-square sense, the difference with the expected trend from the Gaussian model, as it is standard in approaching this problem in industrial settings. Instead, figure 12(c) reports the same trends as in figure 12(a) having normalised the distance from the wind turbine by using two parameters: a virtual origin x_0 and an alternative value of k^*, which has been labelled k_{fit}. The formulation of equation (3.6) used in the remainder of this paper is therefore

$$\frac{\sigma_w}{D} = k_{\text{fit}} \frac{x - x_0}{D} + 0.25\sqrt{\beta}. \tag{3.9}$$

Both the virtual origin x_0 and the alternative wake recovery rate k_{fit} have been obtained as the two parameters that minimise the sum of squared residuals between each measured trend of ΔU and the predicted curve according to equation (3.5), having imposed $r/D = 0$. The use of a virtual origin to describe the evolution of bluff body wakes in turbulence is a widely

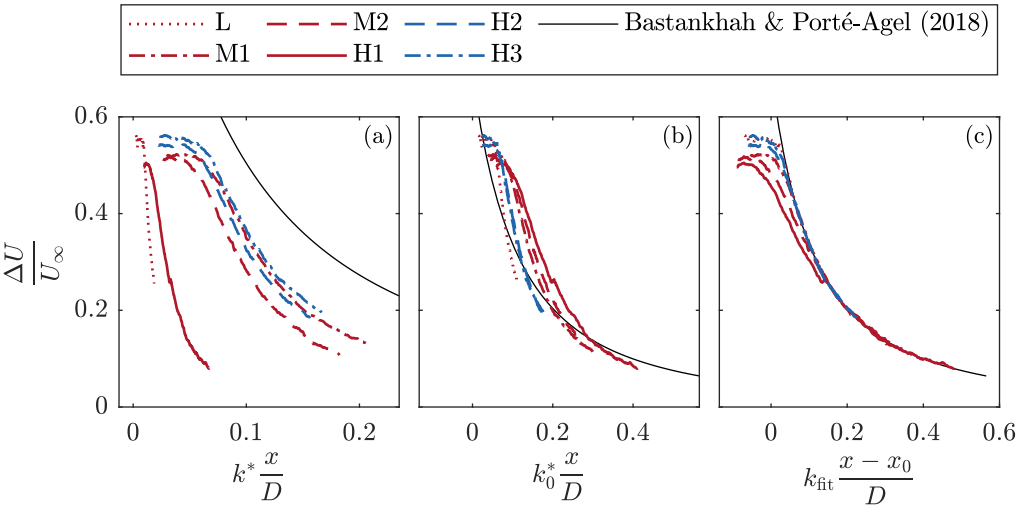

Figure 12: Comparison of the wake velocity deficit trends $\Delta U/U_\infty$ with the trend predicted by Bastankhah and Porté-Agel (2014), assuming $\epsilon_0 = 0.2\sqrt{\beta}$ and k^* inferred from wake profile fitting (*a*), assuming $\epsilon_0 = 0.2\sqrt{\beta}$ and best-fitting k_0^* (*b*), and with the trends obtained by determining the best-fit values of k^* and x_0 assuming $\epsilon_0 = 0.25\sqrt{\beta}$ (*b*). Data for $\lambda = 3.8$.

employed method for other bluff bodies such as porous disks (Rind and Castro 2012a,b; Pal and Sarkar 2015), spheres (Spedding et al. 1996), or even when describing wakes of bodies in turbulent boundary layers (Sakamoto and Arie 1983); this approach has been recently shown to be valid for wakes generated by utility-scale turbines in the atmospheric boundary layer (Neunaber et al. 2022). While the physical meaning of the wake recovery rate is immediate, the plotted trends in figure 12(c) highlight how the virtual origin x_0 is loosely connected to the extent of the interval of x for which the velocity deficit is constant. In this case it can be seen that a collapse, especially for large values of x/D, is obtained regardless of the inflow conditions, improving both on the assumption that k^* can be inferred from the wake diameter growth rate, and on the current industry standard of finding the best-fit k^* and employing no virtual origin. While this shows that the Gaussian wake model can be tuned to predict the wakes of turbines in a wide array of both realistic and non-Kolmogorov-like flows, this also quantifies the effect of turbulence on the wake generated by a wind turbine.

Figure 13 reports the values of the two parameters used, k_{fit} and x_0, for all test cases investigated in this study. For all the turbine operating points, it can be seen that k_{fit} assumes a linear trend with I_∞ if one limits the analysis to the Kolmogorov-like flows. This is in good agreement with previous literature, namely the work of Niayifar and Porté-Agel (2016) and that of Peña et al. (2016) on the Jensen wake model (Jensen 1983), where the authors show how the linear relationship between the wake recovery rate and I_∞ can be recovered assuming the vertical velocity profile is well described by Monin-Obukhov similarity theory (Monin and Obukhov 1954); one must however note that no vertical velocity profile is present in our measurements, and thus the linear relationship between k_{fit} and I_∞ holds even outside the atmospheric boundary layer. The general trend of k_{fit} mimics well what already seen on the wake velocity deficit, for instance in figure 4 and figure 5, where wakes exhibiting higher values of ΔU far from the turbine have low values of k_{fit} and vice-versa.

Instead, the virtual origin x_0 is seen to be less affected by the freestream turbulence conditions: generally, this value is the highest for the low-turbulence case of flow L, regardless of the turbine thrust coefficient, and all other flows exhibit a value of $x_0/D \simeq 2.5$,

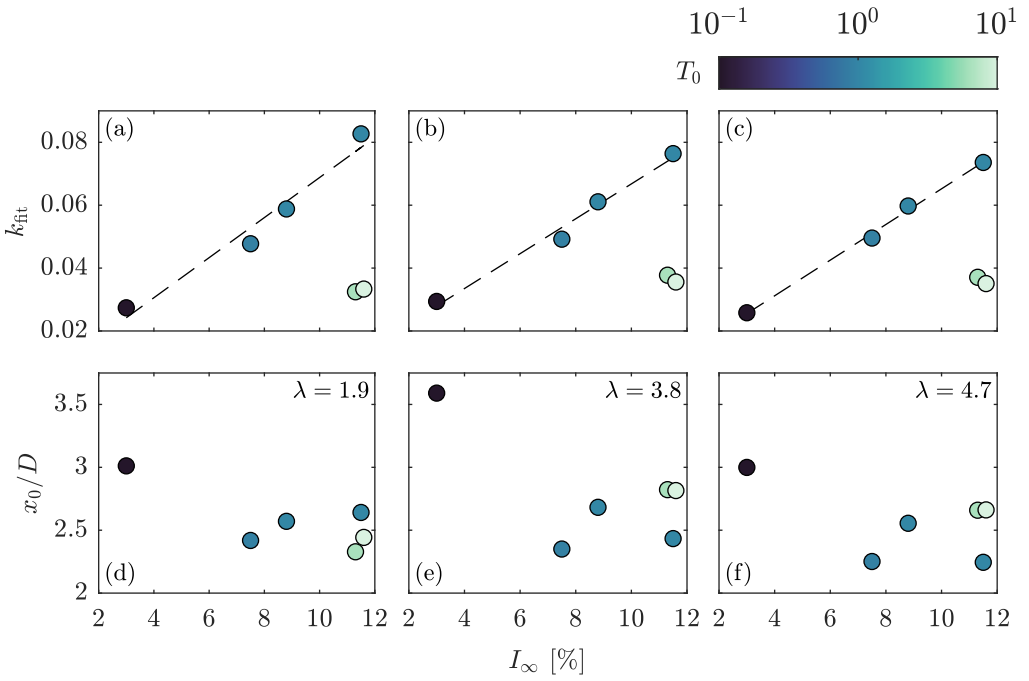

Figure 13: Trends of k_{fit} (a, b, c) and x_0/D (d, e, f) with the freestream turbulence properties I_∞ (horizontal axis) and T_0 (colour axis). Data for $\lambda = 1.9$ (a, d), $\lambda = 3.8$ (b, e), and $\lambda = 4.7$ (c, f).

only moderately affected by C_T and free-stream turbulence. It is also interesting to note that, limiting our attention to high-turbulence flows, the value of x_0 is higher for the non-Kolmogorov flows for the two test cases at high C_T than it is for the Kolmogorov-like flow H1, while this trend appears reversed for the low-C_T test case of $\lambda = 1.9$. However, one must note that the scatter between the values of x_0 obtained for flows H1, H2, and H3 is comparable to the scatter between those of all flows of $T_0 = 1$. It is therefore possible that, while the inclusion of the virtual origin x_0 helps in fitting the curves with the Gaussian wake model, the value of this parameter need not vary with inflow conditions beyond a certain threshold of I_∞.

The parameterisation of the wake in its recovery rate k_{fit} and its virtual origin x_0 also provides a convenient separation between two regions in the wake: in the next section we will argue that the extent of the near wake is loosely related to the trends of x_0 and to the stability of the helical vortex set enveloping the wake. Conversely, one can interpret the value of k_{fit} to be the main parameter that drives the wake evolution for large distances downstream of the turbine, and thus to be representative of the far wake evolution.

3.2. *Influence on near wake extent*

Customarily, the wake of a wind turbine is often divided in two regions: a near wake, where the rotor geometry affects the local velocity field, and a far wake which is instead independent of the turbine geometry and self-similarity is attained (De Cillis et al. 2020); however, seldom a quantitative definition of their extent is given. A number of methods have been presented in literature to estimate the location of the transition between one region and the other, based on considerations on the turbulent kinetic energy content (Sørensen et al. 2015; De Cillis et al. 2020; Wu and Porté-Agel 2012), or on the onset of wake meandering (Howard et al. 2015). It

can be understood that these methods only provide a qualitative estimation of this transition, as there is no hard boundary between the near and the far wake. This however does not mean there is no merit in estimating the near wake length, as trends of these estimations can still provide valuable information as comparison between test cases. In this work, the definition of near-wake length is slightly changed from the one presented by Wu and Porté-Agel (2012): having defined the turbulent kinetic energy as

$$\kappa = \frac{1}{2}\left(\overline{u'^2} + \overline{v'^2} + \overline{w'^2}\right), \tag{3.10}$$

its mean advection is

$$\vec{U} \cdot \nabla\kappa = U\frac{\partial\kappa}{\partial x} + V\frac{\partial\kappa}{\partial y} + W\frac{\partial\kappa}{\partial z}, \tag{3.11}$$

where $\vec{U} = (U; V; W)$ is the time-averaged velocity vector. Note that for steady flows, this is equal to the material derivative of κ:

$$\frac{D\kappa}{Dt} = \frac{\partial\kappa}{\partial t} + \vec{U} \cdot \nabla\kappa = \vec{U} \cdot \nabla\kappa, \tag{3.12}$$

as $\frac{\partial}{\partial t} = 0$ in steady-state conditions. The near wake is then defined as the location where $\frac{D\kappa}{Dt} > 0$ and vice-versa for the far wake. Physically, the interpretations is as follows: as a flow parcel traverses the rotor-swept plane, its turbulent kinetic energy increases under the effect of both the circulation generated by the blades and the vorticity these shed, either as a vortex sheet or as the system of tip- and root-vortices. As the parcel travels downstream, it will cede this to its surrounding; therefore, a positive value of this material derivative denotes that the evolution of the particle is driven by its interaction with the turbine and vice-versa.

As the data collected consists of the two in-plane components of velocity u and v, it is impossible to compute the full turbulent kinetic energy as defined in equation (3.10) as no information is available on w'; similarly, without W, the term relative to the advection of κ in the z-direction cannot be computed. To this reason, the definitions in equations (3.10) and (3.11) have been implemented by assuming that $\frac{v}{w} = O(1)$ and $\frac{\partial}{\partial y} \simeq \frac{\partial}{\partial z}$; thus, the turbulent kinetic energy is estimated as

$$\kappa = \frac{1}{2}\left(\overline{u'^2} + 2\overline{v'^2}\right), \tag{3.13}$$

and its material derivative is estimated as

$$\frac{D\kappa}{Dt} = U\frac{\partial\kappa}{\partial x} + 2V\frac{\partial\kappa}{\partial y}, \tag{3.14}$$

which is an assumption that holds true particularly close to the wake centre, as the wake is somewhat axisymmetric, and gets progressively less so farther from that, as an azimuthal velocity component is introduced as resultant of the torque generated by the blades and the assumption that $v \simeq w$ need not hold (Medici and Alfredsson 2006).

Figure 14 reports the trends of the material derivative of κ with distance from the turbine; this is adimensionalised by the term $\frac{D}{U_\infty^3}$. To reduce the effect of experimental noise on the measurements, the trends reported have been obtained by averaging the value of κ for $|y/D| < 1/2$, equivalent to limiting this analysis only to particles that have traversed the turbine rotor. Moreover, each trend is low-pass filtered to remove all components having a wavelength smaller than $D/2$. The trends highlight a clear distinction between the two regions at positive and negative $\frac{D\kappa}{Dt}$, as well as showing that this value does not trend to a zero value at long distances from the turbine. This is expected and is due to the natural decay

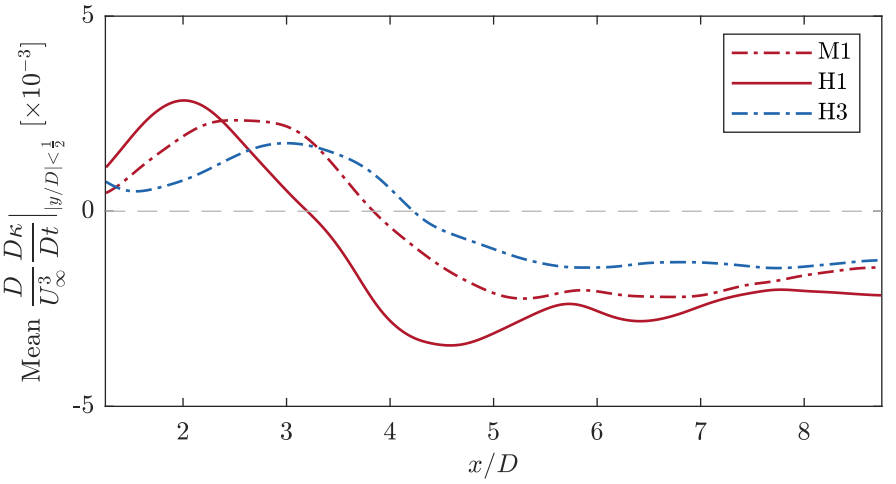

Figure 14: Trends of mean material derivative of turbulent kinetic energy $\frac{D\kappa}{Dt}$ for $|y/D| < \frac{1}{2}$ as a function of the streamwise distance from the turbine for inflows M1, H1, and H3. Turbine operating at $\lambda = 3.8$.

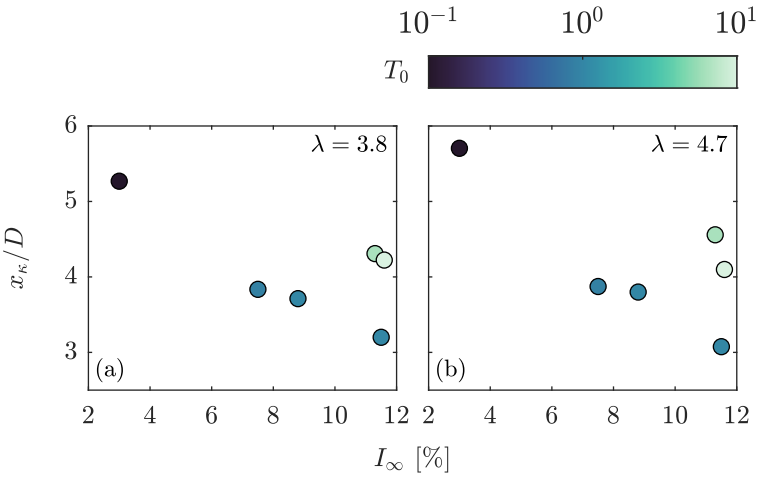

Figure 15: Location of the change of sign x_κ/D in the spatial mean of $D\kappa/Dt$ as a function of the freestream turbulence intensity I_∞ (horizontal axis) and integral timescale T_0 (colour axis), shown for $\lambda = 3.8$ (*a*) and $\lambda = 4.7$ (*b*).

of turbulence with freestream distance, proper of both grid-generated turbulence (Kistler and Vrebalovich 1966; Hearst and Lavoie 2016) and bluff-body wakes (Wygnanski et al. 1986). Defining the value of x at which $\frac{D\kappa}{Dt}$ changes sign as x_κ, one can observe the trends of this parameter with freestream turbulence characteristics in figure 15. Data for $\lambda = 1.7$ is not reported as $\frac{D\kappa}{Dt}$ is negative along the whole domain and no change in sign is observed; for this operating condition, the torque generated by the blades is marginally lower than that at $\lambda = 4.7$ and considerably lower than that at $\lambda = 3.8$ (Gambuzza and Ganapathisubramani 2021): the circulation generated by the blades is therefore lower and so is the intensity of the tip- and root-vortices generated by the blades. This, paired with a lower λ and therefore more spaced vortices, might have led to a less intense interaction between the turbine and the flow traversing the rotor-swept plane. The trends of x_κ are somewhat similar to those of the

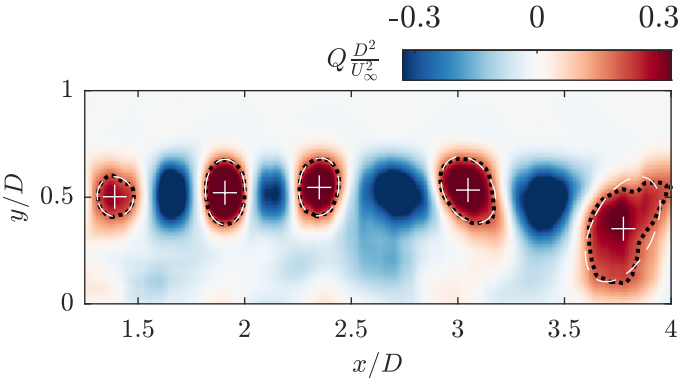

Figure 16: Identification of the tip-vortices location (*white plus signs*) from isocontours of Q-criterion (*black dotted*) approximated with best-fitting ellipses (*white dashed*). Data displayed is that of a representative snapshot obtained at $\lambda = 3.8$ and inflow L.

virtual origin x_0 reported in figure 13(e-f) for the two high-λ test cases: in particular, it can in both cases be seen that the low-I_∞ inflow conditions result simultaneously in a high x_0 and a high x_κ. Moreover, among the three flows at $I_\infty \approx 11.5$ %, the Kolmogorov-like conditions of flow H1 are the ones that result in the lowest values of both x_0 and x_κ. However, focusing one's attention only to the Kolmogorov-like flows at $T_0 \leqslant 1$, x_κ shows a clear decreasing trend that is not readily seen in the values of the virtual origin. This suggests that the changes in value of the virtual origin are broadly affected by the same mechanisms that regulate the near-to-far-wake transition, although x_0 cannot be taken as representative of the transition distance.

To understand the conditions that drive the evolution of the near wake, it is useful to observe the behaviour of the tip-vortices shed by the turbine. Vortex identification from an instantaneous velocity snapshot can be carried out with a number of techniques; in this work, the Q-criterion (Hunt et al. 1988; Jeong and Hussain 1995; Haller 2005) has been employed due to the simplicity of the underlying equations and the ease of adaptation to planar data. For an instantaneous velocity field $\vec{u}(t) = (u(t), v(t))$, the in-plane value of Q is computed as

$$Q = -\frac{1}{2}\left(\left(\frac{\partial u}{\partial x}\right)^2 + 2\frac{\partial u}{\partial y}\frac{\partial v}{\partial x} + \left(\frac{\partial v}{\partial y}\right)^2\right), \tag{3.15}$$

and vortices are individuated as continuous regions in the flow where $Q > 0$. Figure 16 reports the map of Q for a representative velocity snapshot obtained for the operating conditions of $\lambda = 3.8$ and inflow L, along with the methodology used to individuate the location and intensity of individual vortices. Given a computed map of Q, contiguous regions of positive Q are individuated as the regions bounded by iso-lines of Q equal to a certain threshold, which in this case has been chosen as $0.3(D/U_\infty)^2$; the iso-lines are then approximated with the best-fitting ellipse, with the centre of the ellipse being used as the location of the vortex and the value of Q at the centre being an indication of the vortex intensity.

The position of the vortices is shown in figure 17 for four edge-cases, all having the turbine operating at $\lambda = 3.8$. From these, it can be seen how the low turbulence intensity of flow L results in a very coherent and stable train of vortices mostly concentrated around the tip-height line at $y/D = 0.5$, with some small instability setting on at $x/D > 3.5$. For the two Kolmogorov-like inflows at high I_∞, namely M1 and H1, shear layer instability is favoured by the high amount of freestream turbulence and the vortices positions are more erratic: this shear layer instability in turn drives the wake meandering seen in figure 6 for the same two

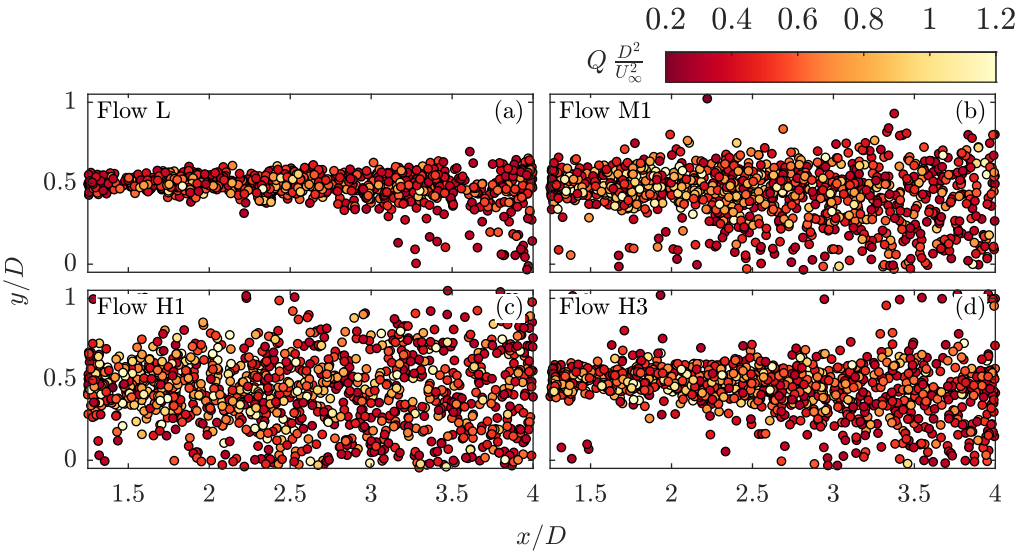

Figure 17: Instantaneous position of the tip-vortices for inflows L (*a*), M1 (*b*), H1 (*c*), and H3 (*d*), coloured by their peak Q. Turbine operating at $\lambda = 3.8$. For clarity, a random subset of 1200 individual vortices is shown for every subfigure.

test cases. The test case of the non-Kolmogorov flow H3 is instead seen, despite the same value of I_∞, to result in an initially more stable shear layer, with the tip-vortices occupying a region close to $y/D = 0.5$, larger than that generated under inflow L but visibly bounded, unlike that of the two previous flows M1 and H1; this initial shear layer stability is possibly connected to the less intense wake meandering observed in figure 6. The mechanisms that drive the breakdown of the tip-vortex set are well known and extensively studied in literature. Ivanell et al. (2010), Sarmast et al. (2014), and Lignarolo et al. (2015) show how at a certain distance from the turbine the phenomenon of leapfrogging, that is the interaction between a vortex and the preceding or following one, contributes to the breakdown of this structure; in particular, Ivanell et al. (2010) shows that the additional perturbations due, for instance, to freestream turbulence, favour the onset of leapfrogging closer to the rotor, which is further confirmed by Sarmast et al. (2014). In the case of the results reported in figure 17, the leapfrogging cannot be directly observed; however, it can be reasonably assumed that the more erratic trajectory of these vortices in the case of inflows M1 and H1 does indeed favour interaction between adjacent vortices closer to the rotor.

It has been previously reported in literature that the presence of the helical vortex set envelopes the wake and prevents transfer of momentum between the wake and the surrounding freestream, thus delaying the wake evolution (Lignarolo et al. 2014, 2015; De Cillis et al. 2020): this suggests that the initial wake evolution is hampered by the presence of a stable shear layer and thus by a train of coherent vortices, which effectively shield the near wake from the freestream. This can be easily visualised, for the test cases here reported, with quadrant analysis to characterise the events on the mean vortices trajectory. At these locations, a $v' < 0$ denotes flow crossing the vortices trajectory from the high-momentum freestream to the wake and $v' > 0$ denotes conversely motion from the wake outwards; simultaneously, $u' > 0$ indicates motion of high-momentum flow and $u' < 0$ indicates that of low-momentum flow. Wake evolution is therefore promoted either by the sweep of high-momentum flow inside the wake, for which $u' > 0$ and $v' < 0$, or by ejection of low-momentum flow from the wake, for which $u' < 0$ and $v' > 0$; vice-versa, wake evolution is hampered by interaction events,

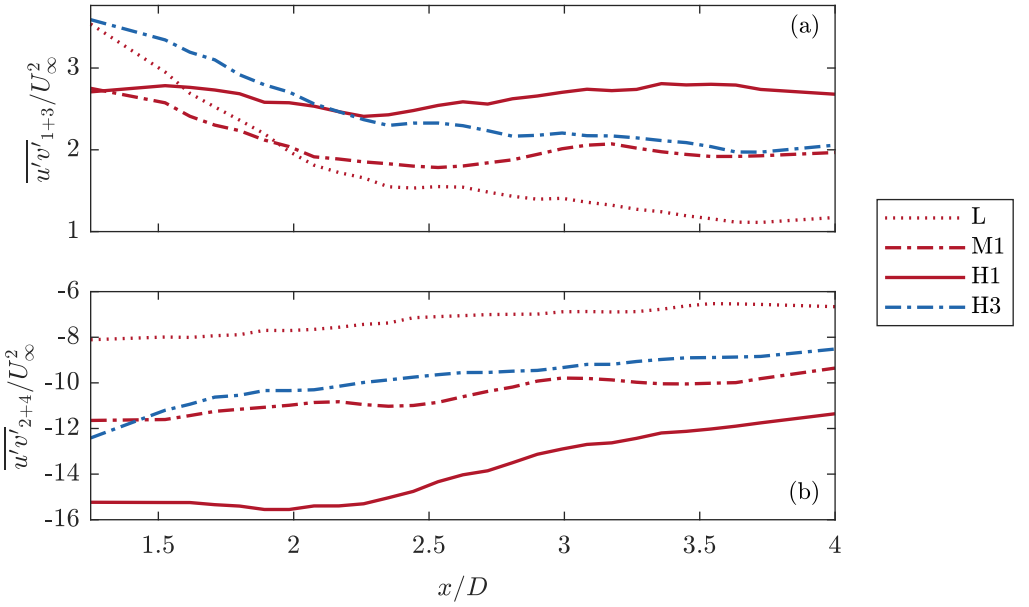

Figure 18: Sum of the contributions to the Reynolds shear stress in the first and third quadrant (*a*) and in the second and fourth quadrant (*b*), on the mean tip-vortices trajectory. Data for inflows L, M1, H1, and H3, and $\lambda = 3.8$.

for which u' and v' have the same sign. Defining thus the individual contributions to the in-plane Reynolds shear stress $\overline{u'v'}$ in each quadrant as

$$\overline{u'v'}_j = \int_{Q_j} u'v' \, P(u', v') \, du' \, dv', \tag{3.16}$$

where Q_j denotes the j-th quadrant and $P(u', v')$ is the joint probability density function for an event in the (u', v')-space. Moreover, one can define

$$\overline{u'v'}_{1+3} = \overline{u'v'}_1 + \overline{u'v'}_3 \tag{3.17}$$

and likewise for $\overline{u'v'}_{2+4}$.

The trends of the quadrant contributions on the mean vortices trajectory are reported in figure 18, divided in events that hamper the wake evolution (figure 18(a)) and those that favour it (figure 18(b)). By observing the trends of the second and fourth quadrant, for which a negative value indicates more intense sweep and ejection events and therefore a faster-evolving wake, one can see that the fast-evolving wake under flow H1 is indeed the one that results in the largest value of $\overline{u'v'}_{2+4}$ and thus in the most intense interaction between freestream and wake. For the Kolmogorov-like flows, the intensity of these events is roughly proportional to the freestream turbulence intensity I_∞; this relationship does however not hold for the non-Kolmogorov test case of inflow H3, which is seen instead to have a value of Q2 and Q4 events slightly lower than those of flow M1, despite the larger I_∞. By instead observing the trends of Q1 and Q3 events, it can be seen that the relationship between events intensity and I_∞ need not necessarily hold close to the wind turbine: in fact, for small values of x/D, flow *L* results in interaction events that are more intense than those developed for inflow M1 and H, despite the much less intense inflow turbulence; this however decays rapidly and by $x/D = 2$ flow L is once again the one for which events intensity is the smallest. It is instead more interesting to observe the intensity of interaction events for flow H3, which are

seen to be more intense than those of flow M1 along the whole of the near wake, and larger than those of flow H1 close to the turbine until $x/D \approx 2.25$.

From the data here presented, it is evident that the main cause of the delayed onset of wake evolution has to be found in the robustness of the train of tip-vortices, which is in turn driven by the shear layer instability. A stable shear layer inhibits sweep and ejection events, and favours interaction events. The effect of freestream turbulence intensity I_∞ on the shear layer stability is non-trivial, as it has been seen that a non-Kolmogorov-like inflow with energy content skewed towards low-frequency contributions results in a more stable shear layer than a Kolmogorov-like flow.

3.3. *Far wake evolution*

While the stability of the enveloping helical vortex structure is consistent with the near-to-far wake transition, this phenomenon does not provide an explanation for the rate at which the wake recovers, and thus for the different values of the wake recovery rate k_{fit} as seen in the previous figure 13. To understand the drivers of wake evolution in the far wake region, it can be useful to approach the Reynolds-averaged Navier-Stokes equations, in particular the one that describes the evolution of the streamwise momentum component: for a steady three-dimensional flow this can be expressed as

$$U\frac{\partial U}{\partial x} + V\frac{\partial U}{\partial y} + W\frac{\partial U}{\partial z} + \frac{\partial \overline{u'^2}}{\partial x} + \frac{\partial \overline{u'v'}}{\partial y} + \frac{\partial \overline{u'w'}}{\partial z} = -\frac{1}{\rho}\frac{\partial P}{\partial x}, \tag{3.18}$$

where the contributions due to viscosity have been neglected as the Reynolds number is high. The momentum equation in the y-direction can be simplified (Townsend 1999) to the expression

$$\frac{\partial \overline{v'^2}}{\partial y} + \frac{\partial \overline{v'w'}}{\partial z} = -\frac{1}{\rho}\frac{\partial P}{\partial y} \tag{3.19}$$

As for the turbulent kinetic energy computation in section 3.2, one can remedy the lack of information on the out-of-plane components of velocity by assuming that $\frac{\partial}{\partial y} \simeq \frac{\partial}{\partial z}$ and $\overline{v'^2} \simeq \overline{w'^2}$. While this is a strong assumption, it can be thought as reasonable especially close to the wake centreline: being the wake generated by the wind turbine roughly axisymmetric, both y and z represent radial directions from the wake axis outwards. With these assumptions, equation (3.18) near the wake centreline can be expressed in the simplified form

$$U\frac{\partial U}{\partial x} = -2V\frac{\partial U}{\partial y} - \frac{\partial(\overline{u'^2} - 2\overline{v'^2})}{\partial x} - 2\frac{\partial \overline{u'v'}}{\partial y} + R, \tag{3.20}$$

where R is a residual term that takes into account the differences between the left- and right-hand side of the equation due to the simplifying assumptions employed in this formulation, and the $-2\overline{v'^2}$ in the second term of the right-hand side derives from equation (3.19): with the simplifying assumption employed, one has

$$2\frac{\partial \overline{v'^2}}{\partial y} = -\frac{1}{\rho}\frac{\partial P}{\partial y} \Rightarrow -\frac{1}{\rho}\frac{\partial P}{\partial x} = 2\frac{\partial \overline{v'^2}}{\partial x} + \frac{1}{\rho}\frac{\partial P_0}{\partial x}, \tag{3.21}$$

with the terms at the right-hand side of the implication sign being obtained by integrating the left-hand side in y and then taking the derivative in x. In particular, P_0 is the integration coefficient that stems from the integration of $\frac{\partial P}{\partial y}$ in y and thus is constant in the vertical direction: for this reason, its evolution in x is due to the presence of a potential pressure gradient due to the facility, which is arbitrarily assumed to be negligible here to simplify the

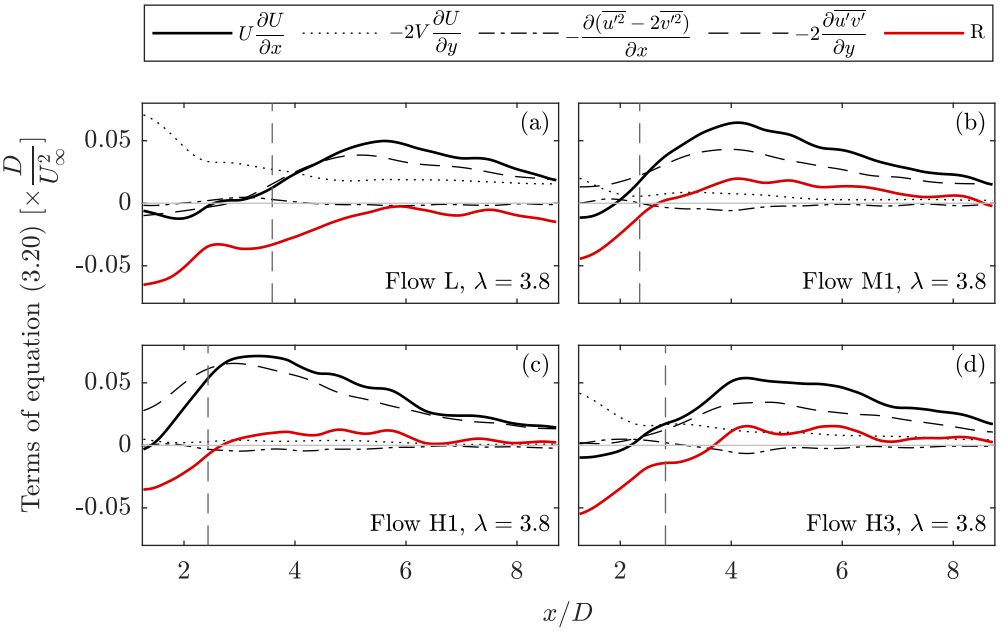

Figure 19: Terms of equation (3.20), made adimensional by multiplication with D/U_∞^2, for the inflows L (*a*), M1 (*b*), H1 (*c*), and H3 (*d*), (*black and red lines*), along with value of x_0 (*dashed vertical line*); turbine operating at $\lambda = 3.8$.

analysis. The variation of the terms of equation (3.20) in x/D is reported, for four test cases having $\lambda = 3.8$, in figure 19, along with the value of the virtual origin computed for each wake. It can be seen that for the cases of high I_∞ (inflows M1, H1, and H3) the dominant term of those at the right-hand side of equation (3.20) is indeed the one relative to the in-plane Reynolds shear stress, as it is often assumed for far wakes (Tennekes and Lumley 1972), and that for $x/D > x_0/D$ the residual R is often small enough to be negligible; this is however not true for the case of the low I_∞ of flow L, for which instead there is a non-negligible contribution of the mean advection term $V\frac{\partial U}{\partial y}$. This is consistent with results previously published in literature, where higher Reynolds shear stresses generated in the turbine wake result in a swifter evolution of the streamwise velocity component (Chamorro and Porté-Agel 2010), or base flows exhibiting a larger Reynolds shear stress upstream of the wind turbine result in a faster wake evolution despite similar values of free-stream I_∞ (Zhang et al. 2013).

Assuming therefore that, at least for the high-I_∞ flows,

$$U\frac{\partial U}{\partial x} \simeq -2\frac{\partial \overline{u'v'}}{\partial y} \tag{3.22}$$

holds true for $x/D > x_0/D$ and on the wake centreline, one can obtain an analytical relationship between the value of the wake recovery rate k^* and the in-plane Reynolds shear stress at the centreline. In fact, noting that

$$U\frac{\partial U}{\partial x} = \frac{1}{2}\frac{\partial U^2}{\partial x}, \tag{3.23}$$

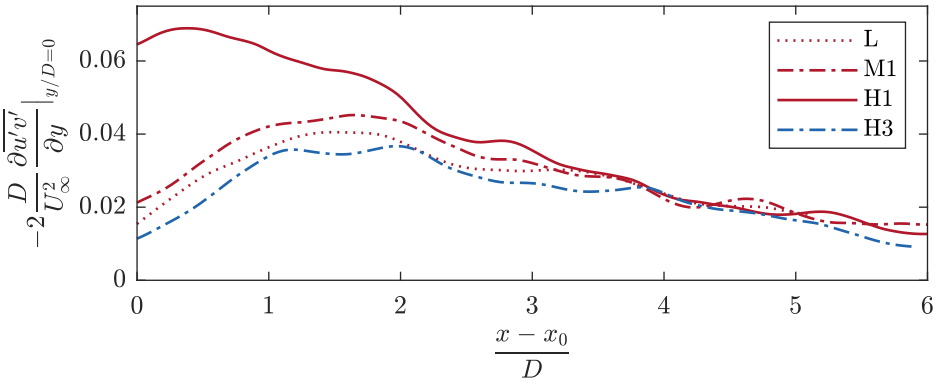

Figure 20: Distribution of the derivative of Reynolds shear stress on the wake centreline, from the location of the virtual origin onwards. Data for $\lambda = 3.8$.

one can integrate equation (3.22) to yield

$$\int_{x_0}^{x_{\mathrm{fw}}} \frac{\partial U^2}{\partial x}\, dx = U_{\mathrm{fw}}^2 - U_{x_0}^2 = -4 \int_{x_0}^{x_{\mathrm{fw}}} \frac{\partial \overline{u'v'}}{\partial y}\, dx, \tag{3.24}$$

where x_{fw} is a far-downstream station, U_{x_0} is the value of U at the virtual origin, and likewise U_{fw} is the value of U downstream of the turbine. The modified formulation of Bastankhah and Porté-Agel (2014) presented in this paper can be used to estimate the values of U in the wake: arbitrarily choosing $x_{\mathrm{fw}} = x_0 + nD$, one has

$$\frac{U_{\mathrm{fw}}^2}{U_\infty^2} = 1 - \frac{C_T}{8(\epsilon_0 + nk^*)^2}, \tag{3.25}$$

$$\frac{U_{x_0}^2}{U_\infty^2} = 1 - \frac{C_T}{8\,\epsilon_0^2}, \tag{3.26}$$

which, substituted in equation (3.24) yield

$$\frac{C_T}{8\,\epsilon_0^2} - \frac{C_T}{8(\epsilon_0 + nk^*)^2} = -4 \int_{x_0}^{x_0+nD} \frac{1}{U_\infty^2} \frac{\partial \overline{u'v'}}{\partial y}\, dx. \tag{3.27}$$

This is a quadratic equation in k^*: its positive solution is found as

$$k^*_{\mathrm{est}} = \frac{\epsilon_0}{n} \left(\sqrt{\frac{C_T}{C_T + 32\, I_{\mathrm{RSS}}\, \epsilon_0^2}} - 1 \right) \tag{3.28}$$

where I_{RSS} refers to the integral of the Reynolds shear stress derivatives at the right-hand side of equation (3.27):

$$I_{\mathrm{RSS}} = \int_{x_0}^{x_0+nD} \frac{1}{U_\infty^2} \frac{\partial \overline{u'v'}}{\partial y}\, dx. \tag{3.29}$$

Figure 20 reports the values of the derivative of the in-plane Reynolds shear stress on the wake centreline, here approximated as the horizontal axis having $y/D = 0$. It can be seen that this quantity is, for the Kolmogorov-like flows, increasing with increasing I_∞. This relationship however does not hold for the non-Kolmogorov-like test case of flow H3, for which the derivative of the Reynolds shear stress is the lowest of all test cases here analysed. Figure 21 reports the fields of the Reynolds shear stress in the turbine wake for

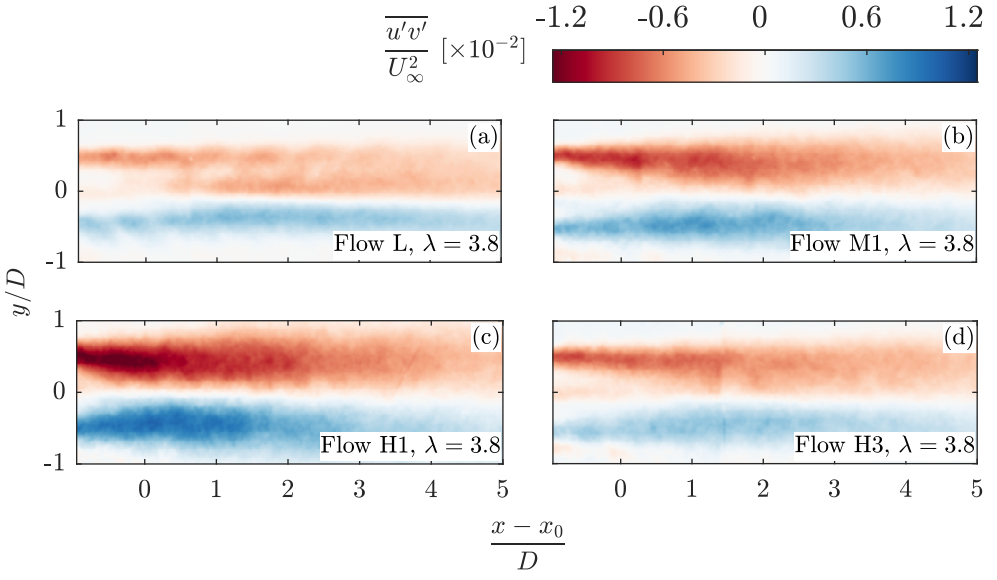

Figure 21: Fields of Reynolds shear stress $\overline{u'v'}$ in the turbine wake for the test cases presented in figure 20.

the test cases corresponding to the test cases presented in figure 20: from these, it can be appreciated that the effect of the freestream conditions on the quantity plotted in figure 20 are indeed representative of a more general and less localised phenomenon. Indeed, it can be appreciated that flow H1 is the test case for which the Reynolds shear stress is the strongest for low values of x, and that the stress in the wake generated by the test cases M1 and H3 are comparable in absolute values. Moreover, one can notice how, for all test cases, the value of this derivative is similar once a large enough distance from the turbine has been covered, such as for $\frac{x-x_0}{D} > 4$, while all differences in these trends are concentrated at small distances from the turbine. This is in accordance with equation (3.22) and the data reported previously in figure 12, which shows that all streamwise velocity deficit trends tend to the same overall shape (and therefore, the same spatial gradient in the streamwise direction) sufficiently far from the turbine.

The values of k_{fit} obtained from fitting the velocity deficit trends have been reported as square markers in figure 22. Alongside these, we present the values of k^*_{est} obtained by multiplying the result of equation (3.28) by 4, as this equation appears to underestimate the actual values of k_{fit} by such a factor. Focusing on the medium- and high-λ cases, it can be appreciated that, with the single exception of the low-I_∞ test case at $\lambda = 3.8$, this equation is able to capture both the linear trend of k^* with I_∞ and the drop in the wake recovery rate for the non-Kolmogorov-like inflow conditions, regardless of the thrust generated by the turbine. However, as it can be seen from figure 22(a), this relationship need not hold for the low-C_T case. In this case as well, however, the linear trend of k^* with I_∞ and the drop for high-T_0 flows are recovered. Therefore, it is reasonable to approximate the wake recovery rate k_{fit} as

$$k_{\text{fit}} \simeq 4\frac{\epsilon_0}{n}\left(\sqrt{\frac{C_T}{C_T + 32\, I_{\text{RSS}}\, \epsilon_0^2}} - 1\right) \tag{3.30}$$

for high-thrust operating conditions and high values of I_∞.

Following this, it can be understood that the driver of the mean wake velocity evolution is the Reynolds shear stress: knowing this, it can be expected that flows with higher values

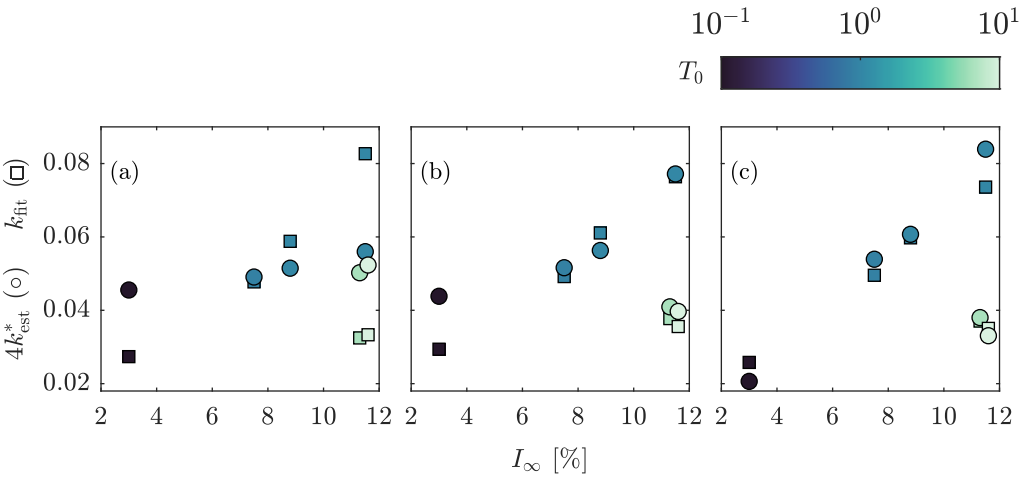

Figure 22: Estimation of k_{fit} from integration of the Reynolds shear stress on the wake trajectory according to equation (3.30) (*round markers*) and comparison with the values found by fitting the wake velocity deficit trends (*square markers*). Data from $\lambda = 1.9$ (*a*), $\lambda = 3.8$ (*b*), and $\lambda = 4.7$ (*c*).

of freestream turbulence intensity result in faster-evolving wakes as they favour a larger content of Reynolds shear stress in the wake, which explains the trend of k^* with I_∞, seen to be linear in literature. A large body of literature (Chamorro et al. 2015; Tobin et al. 2015; Deskos et al. 2020; Gambuzza and Ganapathisubramani 2021) in the last years has shown a relationship between the spectrum of the incoming velocity fluctuations and the power harvested by a turbine from said incoming velocity field, with the turbine harvesting more power for spectra biased towards lower frequency. It can therefore be assumed that, as the turbine harvests power from low-frequency velocity contributions, these will not be present in the wake: in other words, if the turbine acts as a low-pass filter from the point of view of harvested power, it must act as a high-pass filter from the point of view of its wake; this is indeed observed by Tobin and Chamorro (2019), in which the velocity spectra downstream of the turbine are biased towards higher-frequency contributions than those upstream of it. A similar observation is reported by Heisel et al. (2018) for data acquired in the wake of an utility-scale wind turbine. The idea that a turbine acts as to remodulate the spectral content in its wake has been also shown by the LES data by Chatterjee and Peet (2018, 2021), where the authors show that, for an infinite wind farm, the presence of large scales in the freestream favours the transfer of mean kinetic energy from the freestream to the wake, thus hastening the wake recovery and changing the spectral content of the wake. While this would suggest that flows H2 and H3 should result in a faster-evolving wake, a number of differences are present between these works and the present study. For instance, in the case of these cited works, the authors present their conclusions in the frame of an infinite turbine; it is possible that, for an isolated turbine, the mechanism of power extraction dominates over that of mean kinetic energy entrainment. Moreover, the length scales of the eddies generated in Chatterjee and Peet (2018) are at most of $O(10D)$, or equivalently corresponding to inflows with high-energy content at $f\,D/U_\infty = 10^{-1}$. The two high-timescale flows here investigated, namely H2 and H3, instead show peaks in the power spectral distribution at $f\,D/U_\infty = 10^{-2}$, that is one order of magnitude lower than what investigated in the cited works, further suggesting that the mean kinetic energy entrainment mechanics are affected by the freestream content of turbulence in a non-trivial way.

As no time-resolved data is available in the wake of the turbine, the hypothesis that spectra

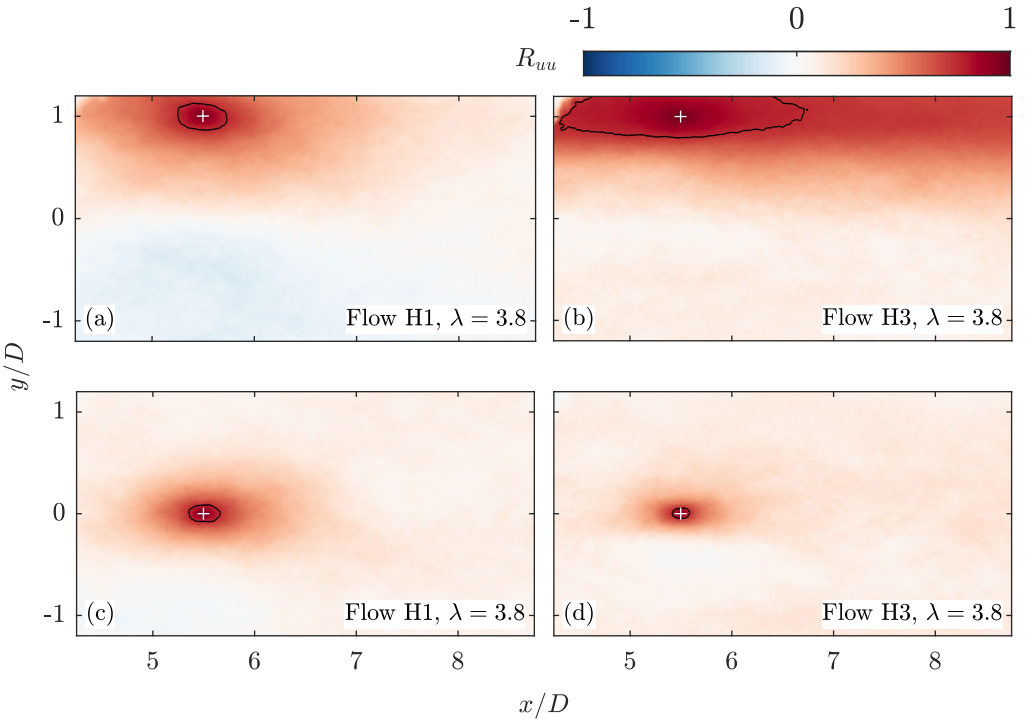

Figure 23: Two-point correlation coefficient R_{uu} maps in the far wake of the turbine operating under base flows H1 (*a*, *c*) and H3 (*b*, *d*), and iso-line of $R_{uu} = 0.75$ (*black line*); fixed point $x_f/D = 5, y_f/D = 1$ (*a*, *b*) and $x_f/D = 5, y_f/D = 0$ (*c*, *d*) (*white plus sign*). Turbine operating at $\lambda = 3.8$.

in the wake are biased towards high-frequency contributions cannot be verified; however, one can quantify the dominant scales in the wake by means of two-point correlation. Defining the two-point correlation coefficient between a fixed point (x_f, y_f) and a generic point (x, y) in the domain as

$$R_{uu} = \frac{\overline{u'(x_f, y_f)\, u'(x, y)}}{\left(\overline{u'^2(x_f, y_f)}\, \overline{u'^2(x, y)}\right)^{1/2}}, \tag{3.31}$$

the value of R_{uu} acts, in space, as analogous to the classical autocorrelation in time for a time-resolved, single-point measurement. Figure 23 reports the value of R_{uu} for the far wake generated by the turbine under inflows H1, which is Kolmogorov-like, and H3, which is not; the points that are chosen as fixed are $(x_f/D = 5.5, y_f/D = 0)$ as representative of the flow in the wake, and $(x_f/D = 5.5, y_f/D = 1)$ for the freestream; moreover, the figure also reports the iso-line of $R_{uu} = 0.75$ for all cases. It can be seen that, for both the Kolmogorov-like inflow conditions of flow H1 and those of flow H3, the correlation decreases by moving from the freestream to the far wake: the characteristic lengths of the presented iso-line reduce both in x and y showing a bias towards lower wavelengths in the wake spectral composition, which can be thought of analogous to the bias towards high-frequency contributions observed by Tobin and Chamorro (2019). Moreover, it can also be observed that, while the changes in R_{uu} are limited in the vicinity of the fixed point for the case of flow H1, the difference between the correlation maps for flow H3 is instead more evident: this does further point towards a clear difference between the spectra of the freestream and the wake for non-Kolmogorov

flows, as the turbine has harvested the low-frequency, high-wavelength contributions in the freestream.

To quantify this phenomenon, one can attempt to define an equivalent turbulence intensity by purposefully filtering out the low-frequency contributions in the freestream velocity power spectral density:

$$I_{\text{filt}}(f_{\text{filt}}) = \left(\frac{1}{U_\infty^2} \int_{f_{\text{filt}}}^{\infty} \phi_u(f)\, df \right)^{1/2}, \tag{3.32}$$

where f_{filt} is the cut-off frequency of an idealised high-pass filter. Tobin et al. (2015) suggests, from comparison between the power spectral densities of the freestream turbulence and the mechanical power generated by the turbine,

$$f_{\text{filt}} = \frac{2Q}{J\omega}, \tag{3.33}$$

where Q is the torque exerted by the turbine on the shaft, J is the rotor moment of inertia, and ω is the rotor angular velocity. Additionally, Li et al. (2022) suggest that side-to-side motions of a turbine excite wake meandering if these come at a Strouhal number $St = fD/U_\infty$ greater than 0.1; there might thus be merit in using a constant

$$f_{\text{filt}} = 0.1 \frac{U_\infty}{D} \tag{3.34}$$

for all test cases. Lastly, if one assumes that the turbine fully converts the low-frequency contributions to the freestream velocity into mechanical power, one could use

$$f_{\text{filt}} = \underset{0.05<St<20}{\text{argmin}} \; (f\phi_u(f)) \tag{3.35}$$

for the non-Kolmogorov-like flows H2 and H3, and $f_{\text{filt}} = 0$ otherwise: this means that $I_{\text{filt}} = I_\infty$ for the Kolmogorov-like inflow conditions. Note that, for both flows H2 and H3, equation (3.35) returns $f_{\text{filt}} \approx 0.1\frac{U_\infty}{D}$: for this reason, the only difference between the approaches of equation (3.34) and equation (3.35) is on whether filtering is applied to the Kolmogorov-like test cases.

Figure 24 shows the values of k_{fit} obtained by fitting the velocity deficit trends of figure 4 as a function of the filtered, equivalent freestream turbulence intensity I_{filt}: the top row employs equation (3.33), the middle row uses equation (3.34) and the bottom row uses equation (3.35) for the non-Kolmogorov-like inflows only, without any filtering of the inflow for the more canonical turbulence cases. The figure shows that, independently of the definition that one employs for f_{filt}, I_{filt} is lower for the non-Kolmogorov-like flows than it is for the more canonical test cases. In particular, using the arbitrary definition of equation (3.35), one recovers the linear trend of k, this time against I_{filt}, that is the current state-of-the-art in the application of analytical wake models in turbulent inflows (Peña et al. 2016; Niayifar and Porté-Agel 2016): this is an additional indicator of a bias towards the remodulation of the wake spectral content by the presence of the turbine, previously seen in literature.

4. Conclusions

This paper has presented measurements of the wake generated by a model-scale wind turbine in a streamwise plane for streamwise distances between $1.25D$ and $8.75D$ downstream of the rotor-swept plane. The freestream turbulence characteristics have been changed by means of an active grid to generate a variety of flows, of which some exhibited the canonical distribution of energy in the frequency domain of Kolmogorov, while others presented artificial contributions at very low frequencies; all flows have been defined by their freestream

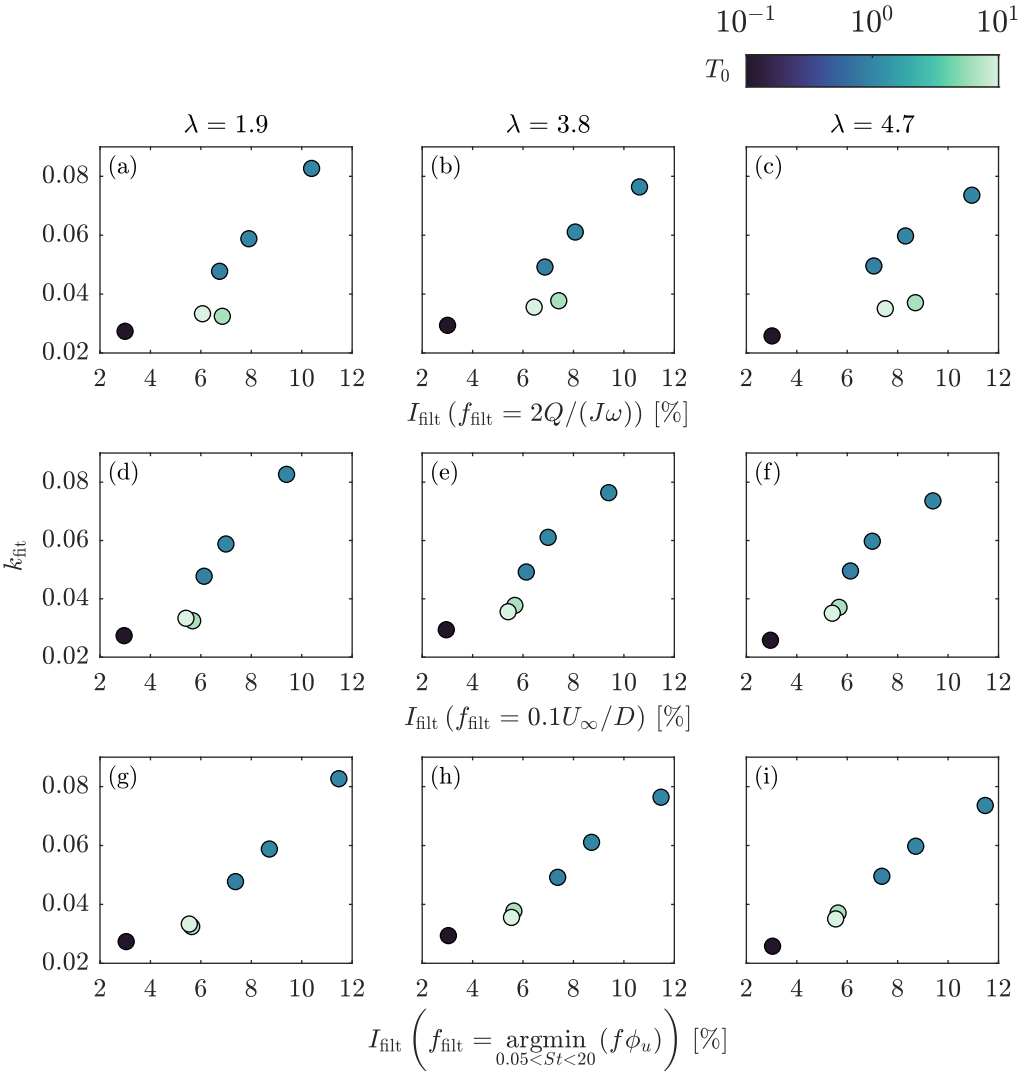

Figure 24: Trends of k_{fit} with the filtered turbulence intensity I_{filt}, for λ = 1.9 (*a, d, g*), λ = 3.8 (*b, e, h*), and λ = 4.7 (*c, f, i*), using three different definitions of f_{filt}.

turbulence intensity I_∞ and their integral timescale T_0. For Kolmogorov-like flows, it has been seen that increasing the turbulence intensity in the freestream results in a wake whose evolution starts closer to the wind turbine rotor, whose recovery is faster and whose overall length is smaller, as shown in previous literature on wakes of both wind turbines and bluff-bodies; highly-turbulent inflows moreover induce more intense wake meandering. Wakes in non-Kolmogorov-like turbulence evolve more slowly, and their evolution starts further away from the turbine, than flows with equivalent or even smaller I_∞. Similarly, the amplitude of the wake meandering motion is reduced for these inflow conditions.

To account for these differences, analytical wake models such as the widespread Gaussian wake model (Bastankhah and Porté-Agel 2014) must be reformulated as a function of two parameters: a virtual origin x_0 and a wake recovery rate k_{fit}. Results show here that k_{fit} varies considerably with the freestream turbulence conditions, while the wake diameter growth rate does not. With these assumptions, namely the presence of a virtual origin and the decoupling

between the wake recovery rate and the wake diameter growth, the Gaussian wake model is excellent at predicting the minimum velocity in the wake. It has furthermore been observed that these two parameters refer to two different regions in the wake, as x_0 is broadly influenced by the near wake length, while k_{fit} instead describes the flow behaviour in the far wake.

In particular, the length of the near wake has been estimated in this work by considerations on the turbulent kinetic energy distribution in the turbine wake: it has been observed that the near wake length is small for high freestream turbulence intensity, and increases both with lower I_∞ and for non-Kolmogorov-like flows, following a trend similar to that of the virtual origin x_0. This trend is seen to be driven by the strength of the shear layer enveloping the wake: this is visualised as the instantaneous location of the tip-vortices shed by the turbine in its rotation, whose trajectories are considerably erratic for high-turbulence Kolmogorov inflows and more steady for low-I_∞ and non-Kolmogorov-like inflows. This change in the onset of shear-layer instability is the main driver of both the wake meandering observed in the far wake and in the length of the near wake. It has in fact been observed that wakes whose shear layers break up sooner are characterised, at the wake boundary, by intense sweep and ejection events, that favour the mixing between freestream and wake by expelling low-momentum flow from the wake and incorporating high-momentum flow from outside the wake. This behaviour is inhibited by long-lasting shear layers: these wakes have lower intensity of sweep and ejection events and higher intensity of interaction events, that are detrimental for the wake evolution. In particular, close to the wind turbine, the intensity of interaction events is the largest for the non-Kolmogorov-like flow at high I_∞ than any other wake here analysed.

The wake recovery rate in the far wake is instead seen to be dominated by the Reynolds shear stress distribution at the wake centreline: it is seen that, for all wakes here investigated except the limit case of low-I_∞ and high power, the analytical relationship $U\frac{\partial U}{\partial x} \simeq -2\frac{\partial \overline{u'v'}}{\partial y}$ holds true at the wake centreline. This relationship between the mean wake velocity and the in-plane Reynolds shear stress component has been leveraged to express an analytical relationship between the wake recovery rate k_{fit} and the distribution of Reynolds shear stress; experimental data shows this relationship to hold true for the cases of high turbine thrust, while it is less accurate for the low-thrust test cases. Non-Kolmogorov-like flows are seen to result in slower-evolving wakes as these generate a lower value of Reynolds shear stress at the wake centreline: this behaviour is connected to the phenomenon for which the turbine is shown to harvest more power from the non-Kolmogorov-like flows, thus harvesting a larger fraction of the incoming turbulent kinetic energy from the freestream. This in literature is seen as a bias of the turbulence spectra in the wake towards higher frequency contributions; in this work, this is shown as a large difference in the two-point correlation coefficient R_{uu} between freestream and wake for the non-Kolmogorov-like flow, a difference which is not evident for the classical Kolmogorov-like inflow conditions. Moreover, it has been seen that the linear trend between the wake recovery rate k_{fit} and the freestream turbulence intensity I_∞ can be recovered for the non-Kolmogorov-like flows if one excludes the contributions of low-frequency components from the computation of I_∞. In this work, this is shown by defining a filtered freestream turbulence intensity I_{filt} which is equivalent to I_∞ for canonical Kolmogorov inflows, and arbitrarily excludes low-frequency contributions for non-Kolmogorov-like flows; the trend if k_{fit} against I_{filt} is linear for all operating conditions analysed in this study. Results included in this work have also shown that an alternative definition of I_{filt}, in which all low-frequency contributions are filtered out of both Kolmogorov- and non-Kolmogorov like inflows is not sufficient to recover the linear trend of k_{fit} with I_{filt}: this highlights how the wake behaviour is tied to the low-pass characteristics of the turbine when converting turbulent velocity fluctuations to mechanical power.

Acknowledgements. The authors would like to thank the anonymous reviewers for their input to the original content of the manuscript, which has undoubtedly improved the quality of the final version.

Funding. This research did not receive any specific grant from funding agencies in the public, commercial, or not-for-profit sectors. The Ph.D. scholarship for author S.G. was provided by the University of Southampton.

Declaration of interests. The authors report no conflict of interest.

Data availability statement. The instantaneous velocity snapshots acquired during this study can be found at https://doi.org/10.5258/SOTON/D2197. The scripts necessary to reproduce the data reduction steps and the plots presented here are accessible at https://doi.org/10.5258/SOTON/D2583.

Author ORCID. Stefano Gambuzza https://orcid.org/0000-0001-9070-6901; Bharathram Ganapathisubramani https://orcid.org/0000-0001-9817-0486

REFERENCES

S. Aubrun, M. Bastankhah, R. Cal, B. Conan, R. Hearst, D. Hoek, M. Hölling, M. Huang, C. Hur, B. Karlsen, I. Neunaber, M. Obligado, J. Peinke, M. Percin, L. Saetran, P. Schito, B. Schliffke, D. Sims-Williams, O. Uzol, M. Vinnes, and A. Zasso. Round-robin tests of porous disc models. Journal of Physics: Conference Series, 1256:012004, July 2019. ISSN 1742-6588. .

E. Barlas, S. Buckingham, and J. van Beeck. Roughness Effects on Wind-Turbine Wake Dynamics in a Boundary-Layer Wind Tunnel. Boundary-Layer Meteorol, 158(1):27–42, Jan. 2016. ISSN 1573-1472. .

R. Barthelmie, O. F. Hansen, K. Enevoldsen, J. Højstrup, S. Frandsen, S. Pryor, S. Larsen, M. Motta, and P. Sanderhoff. Ten Years of Meteorological Measurements for Offshore Wind Farms. Journal of Solar Energy Engineering, 127(2):170–176, Apr. 2005. ISSN 0199-6231. .

R. J. Barthelmie and L. E. Jensen. Evaluation of wind farm efficiency and wind turbine wakes at the Nysted offshore wind farm. Wind Energy, 13(6):573–586, May 2010. ISSN 10954244. .

M. Bastankhah and F. Porté-Agel. A new analytical model for wind-turbine wakes. Renewable Energy, 70: 116–123, Oct. 2014. ISSN 0960-1481. .

T. Blackmore, W. M. J. Batten, G. U. Műller, and A. S. Bahaj. Influence of turbulence on the drag of solid discs and turbine simulators in a water current. Experiments in Fluids, 55(1):1637, Jan. 2014. ISSN 0723-4864. .

F. Carbajo Fuertes, C. D. Markfort, and F. Porté-Agel. Wind Turbine Wake Characterization with Nacelle-Mounted Wind Lidars for Analytical Wake Model Validation. Remote Sensing, 10(5):668, May 2018. .

I. Castro. Wake characteristics of two-dimensional perforated plates normal to an air-stream. Journal of Fluid Mechanics, 46(3):599–609, 1971. .

L. P. Chamorro and F. Porté-Agel. A Wind-Tunnel Investigation of Wind-Turbine Wakes: Boundary-Layer Turbulence Effects. Boundary-Layer Meteorology, 132(1):129–149, July 2009. ISSN 0006-8314. .

L. P. Chamorro and F. Porté-Agel. Effects of Thermal Stability and Incoming Boundary-Layer Flow Characteristics on Wind-Turbine Wakes: A Wind-Tunnel Study. Boundary-Layer Meteorology, 136 (3):515–533, Sept. 2010. ISSN 0006-8314. .

L. P. Chamorro, R. E. A. Arndt, and F. Sotiropoulos. Reynolds number dependence of turbulence statistics in the wake of wind turbines. Wind Energy, 15(5):733–742, July 2012. ISSN 10954244. .

L. P. Chamorro, S.-J. Lee, D. Olsen, C. Milliren, J. Marr, R. E. A. Arndt, and F. Sotiropoulos. Turbulence effects on a full-scale 2.5 MW horizontal-axis wind turbine under neutrally stratified conditions. Wind Energy, 18(2):339–349, Feb. 2015. ISSN 10954244. .

T. Chatterjee and Y. T. Peet. Contribution of large scale coherence to wind turbine power: A large eddy simulation study in periodic wind farms. Phys. Rev. Fluids, 3(3):034601, Mar. 2018. .

T. Chatterjee and Y. T. Peet. Streamwise inhomogeneity of spectra and vertical coherence of turbulent motions in a finite-size wind farm. Phys. Rev. Fluids, 6(11):114601, Nov. 2021. .

K. T. Christensen. The influence of peak-locking errors on turbulence statistics computed from PIV ensembles. Experiments in Fluids, 36(3):484–497, Mar. 2004. ISSN 0723-4864, 1432-1114. .

M. B. Christiansen and C. B. Hasager. Wake effects of large offshore wind farms identified from satellite SAR. Remote Sensing of Environment, 98(2):251–268, Oct. 2005. ISSN 0034-4257. .

A. Crespo and J. Hernández. Turbulence characteristics in wind-turbine wakes. Journal of Wind Engineering and Industrial Aerodynamics, 61(1):71–85, June 1996. ISSN 0167-6105. .

T. Dasari, Y. Wu, Y. Liu, and J. Hong. Near-wake behaviour of a utility-scale wind turbine. Journal of Fluid Mechanics, 859:204–246, Jan. 2019. ISSN 0022-1120. .

G. De Cillis, S. Cherubini, O. Semeraro, S. Leonardi, and P. De Palma. POD-based analysis of a wind turbine wake under the influence of tower and nacelle. Wind Energy, 24(n/a), 2020. ISSN 1099-1824. .

I. V. der Hoven. Power spectrum of horizontal wind speed in the frequency range from 0.0007 to 900 cycles per hour. Journal of the Atmospheric Sciences, 14(2):160–164, Apr. 1957. ISSN 1520-0469. .

G. Deskos, G. S. Payne, and B. Gaurier. On the spectral behaviour of the turbulence-driven power fluctuations of horizontal-axis turbines. Journal of Fluid Mechanics, 904(A13):13–14, 2020. .

E. Dogan, R. E. Hanson, and B. Ganapathisubramani. Interactions of large-scale free-stream turbulence with turbulent boundary layers. Journal of Fluid Mechanics, 802:79–107, Sept. 2016. ISSN 0022-1120. .

D. Elliott and J. Cadogan. Effects of wind shear and turbulence on wind turbine power curves. In 1990 European Community Wind Energy Conference and Exhibition, Madrid, Spain, 1990.

G. España, S. Aubrun, S. Loyer, and P. Devinant. Spatial study of the wake meandering using modelled wind turbines in a wind tunnel. Wind Energy, 14(7):923–937, 2011. ISSN 1099-1824. .

D. Foti, X. Yang, F. Campagnolo, D. Maniaci, and F. Sotiropoulos. Wake meandering of a model wind turbine operating in two different regimes. Phys. Rev. Fluids, 3(5):054607, May 2018. .

D. Foti, X. Yang, L. Shen, and F. Sotiropoulos. Effect of wind turbine nacelle on turbine wake dynamics in large wind farms. Journal of Fluid Mechanics, 869:1–26, June 2019. ISSN 0022-1120. .

S. Frandsen and R. Barthelmie. Local Wind Climate within and Downwind of Large Offshore Wind Turbine Clusters. Wind Engineering, 26(1):51–58, Jan. 2002. ISSN 0309-524X. .

S. Frandsen, R. J. Barthelmie, S. Pryor, O. Rathmann, S. Larsen, J. Højstrup, and M. Thøgersen. Analytical modelling of wind speed deficit in large offshore wind farms. Wind Energy, 9(1-2):39–53, Jan. 2006. ISSN 1095-4244. .

S. Gambuzza and B. Ganapathisubramani. The effects of free-stream turbulence on the performance of a model wind turbine. Journal of Renewable and Sustainable Energy, 13(2):023304, Mar. 2021. .

G. Haller. An objective definition of a vortex. Journal of Fluid Mechanics, 525:1–26, Feb. 2005. ISSN 1469-7645, 0022-1120. .

R. Hearst and B. Ganapathisubramani. Quantification and adjustment of pixel-locking in particle image velocimetry. Experiments in Fluids, 56(10):191, Oct. 2015. ISSN 0723-4864. .

R. Hearst and B. Ganapathisubramani. Tailoring incoming shear and turbulence profiles for lab-scale wind turbines. Wind Energy, 20(12):2021–2035, Dec. 2017. ISSN 10954244. .

R. J. Hearst and P. Lavoie. Effects of multi-scale and regular grid geometries on decaying turbulence. Journal of Fluid Mechanics, 803:528–555, Sept. 2016. ISSN 0022-1120. .

R. J. Hearst, G. Gomit, and B. Ganapathisubramani. Effect of turbulence on the wake of a wall-mounted cube. Journal of Fluid Mechanics, 804:513–530, Oct. 2016. ISSN 0022-1120, 1469-7645. .

M. Heisel, J. Hong, and M. Guala. The spectral signature of wind turbine wake meandering: A wind tunnel and field-scale study. Wind Energy, 21(9):715–731, Sept. 2018. ISSN 10954244. .

K. B. Howard, A. Singh, F. Sotiropoulos, and M. Guala. On the statistics of wind turbine wake meandering: An experimental investigation. Physics of Fluids, 27(7):075103, July 2015. ISSN 1070-6631. .

J. C. R. Hunt, A. A. Wray, and P. Moin. Eddies, Streams, and Convergence Zones in Turbulent Flows. In Center for Turbulence Research Proceedings of the Summer Program 1988, 1988.

T. Ishihara and G. W. Qian. A new Gaussian-based analytical wake model for wind turbines considering ambient turbulence intensities and thrust coefficient effects. Journal of Wind Engineering and Industrial Aerodynamics, 2018. ISSN 01676105. .

S. Ivanell, R. Mikkelsen, J. N. Sørensen, and D. Henningson. Stability analysis of the tip vortices of a wind turbine. Wind Energy, 13(8):705–715, 2010. ISSN 1099-1824. .

N. Jensen. A Note on Wind Generator Interaction. Risø National Laboratory, 1983. ISBN 87-550-0971-9.

J. Jeong and F. Hussain. On the identification of a vortex. Journal of Fluid Mechanics, 285:69–94, Feb. 1995. ISSN 1469-7645, 0022-1120. .

S. Kang, X. Yang, and F. Sotiropoulos. On the onset of wake meandering for an axial flow turbine in a turbulent open channel flow. Journal of Fluid Mechanics, 744:376–403, Apr. 2014. ISSN 0022-1120, 1469-7645. .

A. L. Kistler and T. Vrebalovich. Grid turbulence at large Reynolds numbers. Journal of Fluid Mechanics, 26(01):37, Sept. 1966. ISSN 0022-1120. .

A. N. Kolmogorov. The local structure of turbulence in incompressible viscous fluid for very large Reynolds numbers. Doklady Akademii Nauk SSSR, 30:301, 1941. .

L. Li, R. Hearst, M. Ferreira, and B. Ganapathisubramani. The near-field of a lab-scale wind turbine in tailored turbulent shear flows. Renewable Energy, 149:735–748, Apr. 2020. ISSN 09601481. .

Z. Li, G. Dong, and X. Yang. Onset of wake meandering for a floating offshore wind turbine under side-to-side motion. Journal of Fluid Mechanics, 934:A29, Mar. 2022. ISSN 0022-1120, 1469-7645. .

L. Lignarolo, D. Ragni, C. Krishnaswami, Q. Chen, C. Simão Ferreira, and G. van Bussel. Experimental analysis of the wake of a horizontal-axis wind-turbine model. Renewable Energy, 70:31–46, Oct. 2014. ISSN 09601481. .

L. E. M. Lignarolo, D. Ragni, F. Scarano, C. J. Simão Ferreira, and G. J. W. van Bussel. Tip-vortex instability and turbulent mixing in wind-turbine wakes. Journal of Fluid Mechanics, 781:467–493, Oct. 2015. ISSN 0022-1120, 1469-7645. .

P. B. S. Lissaman. Energy Effectiveness of Arbitrary Arrays of Wind Turbines. Journal of Energy, 3(6): 323–328, 1979. ISSN 0146-0412. .

H. Makita. Realization of a large-scale turbulence field in a small wind tunnel. Fluid Dynamics Research, 8:53–64, Oct. 1991. ISSN 0169-5983. .

D. Medici and P. H. Alfredsson. Measurements on a wind turbine wake: 3D effects and bluff body vortex shedding. Wind Energy, 9(3):219–236, May 2006. ISSN 1095-4244. .

A. S. Monin and A. M. Obukhov. Basic laws of turbulent mixing in the surface layer of the atmosphere. Contrib. Geophys. Inst. Acad. Sci. USSR, 151(163):163–187, 1954.

P. Mycek, B. Gaurier, G. Germain, G. Pinon, and E. Rivoalen. Experimental study of the turbulence intensity effects on marine current turbines behaviour. Part I: One single turbine. Renewable Energy, 66:729–746, June 2014. ISSN 09601481. .

I. Neunaber, M. Hölling, R. J. A. M. Stevens, G. Schepers, and J. Peinke. Distinct Turbulent Regions in the Wake of a Wind Turbine and Their Inflow-Dependent Locations: The Creation of a Wake Map. Energies, 13(20):5392, Jan. 2020. ISSN 1996-1073. .

I. Neunaber, M. Hölling, J. Whale, and J. Peinke. Comparison of the turbulence in the wakes of an actuator disc and a model wind turbine by higher order statistics: A wind tunnel study. Renewable Energy, 179:1650–1662, Dec. 2021. ISSN 0960-1481. .

I. Neunaber, J. Peinke, and M. Obligado. Application of the Townsend–George theory for free shear flows to single and double wind turbine wakes–a wind tunnel study. Wind Energy Science, 7(1):201–219, 2022. .

A. Niayifar and F. Porté-Agel. Analytical Modeling of Wind Farms: A New Approach for Power Prediction. Energies, 9(9):741, Sept. 2016. ISSN 1996-1073. .

A. Pal and S. Sarkar. Effect of external turbulence on the evolution of a wake in stratified and unstratified environments. J. Fluid Mech., 772:361–385, June 2015. ISSN 0022-1120, 1469-7645. .

A. Peña, R. Floors, A. Sathe, S.-E. Gryning, R. Wagner, M. S. Courtney, Xiaoli. G. Larsén, A. N. Hahmann, and C. B. Hasager. Ten Years of Boundary-Layer and Wind-Power Meteorology at Høvsøre, Denmark. Boundary-Layer Meteorology, 158(1):1–26, Jan. 2016. ISSN 0006-8314. .

R. E. Poorte and A. Biesheuvel. Experiments on the motion of gas bubbles in turbulence generated by an active grid. Journal of Fluid Mechanics, 461:127–154, June 2002. ISSN 0022-1120. .

S. B. Pope. Turbulent Flows. Cambridge University Press, Cambridge ; New York, 2000. ISBN 978-0-521-59125-6 978-0-521-59886-6.

S. B. Pope and J. H. Whitelaw. The calculation of near-wake flows. Journal of Fluid Mechanics, 73(1): 9–32, Jan. 1976. ISSN 1469-7645, 0022-1120. .

E. Rind and I. P. Castro. On the effects of free-stream turbulence on axisymmetric disc wakes. Experiments in Fluids, 53(2):301–318, Aug. 2012a. ISSN 0723-4864. .

E. Rind and I. P. Castro. Direct numerical simulation of axisymmetric wakes embedded in turbulence. J. Fluid Mech., 710:482–504, Nov. 2012b. ISSN 0022-1120, 1469-7645. .

H. Sakamoto and M. Arie. Vortex shedding from a rectangular prism and a circular cylinder placed vertically in a turbulent boundary layer. Journal of Fluid Mechanics, 126:147–165, Jan. 1983. ISSN 1469-7645, 0022-1120. .

S. Sarmast, R. Dadfar, R. F. Mikkelsen, P. Schlatter, S. Ivanell, J. N. Sørensen, and D. S. Henningson. Mutual inductance instability of the tip vortices behind a wind turbine. Journal of Fluid Mechanics, 755:705–731, Sept. 2014. ISSN 0022-1120, 1469-7645. .

N. S. Sharp, S. Neuscamman, and Z. Warhaft. Effects of large-scale free stream turbulence on a turbulent boundary layer. Physics of Fluids, 21(9):095105, Sept. 2009. ISSN 1070-6631. .

Y. Sheinman and A. Rosen. A dynamic model of the influence of turbulence on the power output of a wind

turbine. Journal of Wind Engineering and Industrial Aerodynamics, 39(1-3):329–341, Jan. 1992. ISSN 01676105. .

A.-S. Smedman-Högström and U. Högström. Spectral Gap in Surface-Layer Measurements. Journal of the Atmospheric Sciences, 32(2):340–350, Feb. 1975. ISSN 0022-4928, 1520-0469. .

J. N. Sørensen, R. F. Mikkelsen, D. S. Henningson, S. Ivanell, S. Sarmast, and S. J. Andersen. Simulation of wind turbine wakes using the actuator line technique. Philosophical Transactions of the Royal Society A: Mathematical, Physical and Engineering Sciences, 373(2035):20140071, Feb. 2015. .

G. R. Spedding, F. K. Browand, and A. M. Fincham. Turbulence, similarity scaling and vortex geometry in the wake of a towed sphere in a stably stratified fluid. Journal of Fluid Mechanics, 314:53–103, May 1996. ISSN 1469-7645, 0022-1120. .

H. Tennekes and J. L. Lumley. A First Course in Turbulence. MIT Press, Cambridge, Mass, 1972. ISBN 978-0-262-20019-6.

N. Tobin and L. P. Chamorro. Modulation of turbulence scales passing through the rotor of a wind turbine. Journal of Turbulence, 20(1):21–31, Jan. 2019. .

N. Tobin, H. Zhu, and L. P. Chamorro. Spectral behaviour of the turbulence-driven power fluctuations of wind turbines. Journal of Turbulence, 16(9):832–846, Sept. 2015. ISSN 1468-5248. .

A. A. Townsend. The Structure of Turbulent Shear Flow. Cambridge Monographs on Mechanics and Applied Mathematics. Cambridge Univ. Pr, Cambridge, 2. ed., transferred to digital printing edition, 1999. ISBN 978-0-521-29819-3 978-0-521-20710-2.

N. Troldborg, J. N. Sorensen, and R. Mikkelsen. Numerical simulations of wake characteristics of a wind turbine in uniform inflow. Wind Energy, 13(1):86–99, Jan. 2010. ISSN 10954244. .

M. Türk and S. Emeis. The dependence of offshore turbulence intensity on wind speed. Journal of Wind Engineering and Industrial Aerodynamics, 98(8):466–471, Aug. 2010. ISSN 0167-6105. .

M. S. Uberoi and P. Freymuth. Turbulent Energy Balance and Spectra of the Axisymmetric Wake. The Physics of Fluids, 13(9):2205–2210, Sept. 1970. ISSN 0031-9171. .

L. Vermeer, J. Sørensen, and A. Crespo. Wind turbine wake aerodynamics. Progress in Aerospace Sciences, 39(6-7):467–510, Aug. 2003. ISSN 03760421. .

M. K. Vinnes, S. Gambuzza, B. Ganapathisubramani, and R. J. Hearst. The far wake of porous disks and a model wind turbine: Similarities and differences assessed by hot-wire anemometry. Journal of Renewable and Sustainable Energy, 14(2):023304, Mar. 2022. .

R. Wagner, M. Courtney, J. Gottschall, and P. Lindelöw-Marsden. Accounting for the speed shear in wind turbine power performance measurement. Wind Energy, 14(8):993–1004, Nov. 2011. ISSN 10954244. .

B. Wieneke. PIV uncertainty quantification from correlation statistics. Meas. Sci. Technol., 26(7):074002, June 2015. ISSN 0957-0233. .

Y.-T. Wu and F. Porté-Agel. Atmospheric Turbulence Effects on Wind-Turbine Wakes: An LES Study. Energies, 5(12):5340–5362, Dec. 2012. ISSN 1996-1073. .

I. Wygnanski, F. Champagne, and B. Marasli. On the large-scale structures in two-dimensional, small-deficit, turbulent wakes. Journal of Fluid Mechanics, 168(-1):31, July 1986. ISSN 0022-1120. .

W. Zhang, C. D. Markfort, and F. Porté-Agel. Wind-Turbine Wakes in a Convective Boundary Layer: A Wind-Tunnel Study. Boundary-Layer Meteorology, 146(2):161–179, Feb. 2013. ISSN 0006-8314. .